BAMS Article

Advances in Land Surface Models and Indicators for Drought Monitoring and Prediction

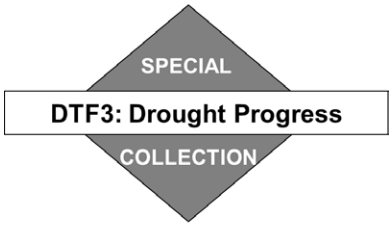

Christa D. Peters-Lidard, David M. Mocko, Lu Su,
Dennis P. Lettenmaier, Pierre Gentine, and Michael Barlage

ABSTRACT: Millions of people across the globe are affected by droughts every year, and recent droughts have highlighted the considerable agricultural impacts and economic costs of these events. Monitoring the state of droughts depends on integrating multiple indicators that each capture particular aspects of hydrologic impact and various types and phases of drought. As the capabilities of land surface models and remote sensing have improved, important physical processes such as dynamic, interactive vegetation phenology, groundwater, and snowpack evolution now support a range of drought indicators that better reflect coupled water, energy, and carbon cycle processes. In this work, we discuss these advances, including newer classes of indicators that can be applied to improve the characterization of drought onset, severity, and duration. We utilize a new model-based drought reconstruction to illustrate the role of dynamic phenology and groundwater in drought assessment. Further, through case studies on flash droughts, snow droughts, and drought recovery, we illustrate the potential advantages of advanced model physics and observational capabilities, especially from remote sensing, in characterizing droughts.

KEYWORDS: Drought; Hydrometeorology; Land surface model; Precipitation; Snowpack; Soil moisture; Vegetation; Vegetation-atmosphere interactions

https://doi.org/10.1175/BAMS-D-20-0087.1
Corresponding author: Christa D. Peters-Lidard, christa.d.peters-lidard@nasa.gov
In final form 23 February 2021

AFFILIATIONS: Peters-Lidard—Earth Sciences Division, NASA Goddard Space Flight Center, Greenbelt, Maryland; **Mocko**—Science Applications International Corporation, Hydrological Sciences Laboratory, NASA Goddard Space Flight Center, Greenbelt, Maryland; **Su and Lettenmaier**—Department of Geography, University of California, Los Angeles, Los Angeles, California; **Gentine**—Department of Earth and Environmental Engineering, and Earth Institute, Columbia University, New York, New York; **Barlage***—Research Applications Laboratory, National Center for Atmospheric Research, Boulder, Colorado

***CURRENT AFFILIATION**—Environmental Modeling Center, NOAA/National Centers for Environmental Prediction, College Park, Maryland

Drought events causing over one billion dollars in damage occur, on average, nearly every year in the contiguous United States (CONUS). Event-specific costs often reach annual levels of $4–7 billion (e.g., the 2014–15 western drought) and sometimes as high as $30 billion (e.g., calendar year 2012 losses from the drought in the central and western United States). The magnitude, breadth, and profound lasting effect of these events on social and economic systems necessitates attention from local, state, regional, and national entities that have responsibility for providing, maintaining, and planning water resources and supplying relevant information.

Monitoring the state of drought depends on integrating and discerning between myriad indicators of the water cycle (Keyantash and Dracup 2002). Dozens of indicators are in common use (e.g., Heim 2002; Svoboda and Fuchs 2017), and each indicator captures particular aspects of hydrologic variability and various types and phases of drought, such as meteorological, agricultural, and hydrological; however, no single indicator is comprehensive. These indicators rely on a diverse array of data sources, including remote sensing, in situ measurements, and human observation, for directly measured quantities such as precipitation, temperature, soil moisture, and streamflow and indirectly estimated quantities such as vegetation biomass and evapotranspiration. Drought indicators form the foundation for drought monitoring (Svoboda 2000) and prediction (Sheffield et al. 2014; Dai 2013), and recent advances in understanding have underscored the need to consider more complex and realistic physical processes when developing these indicators. The goal of this paper is to discuss the technical state of drought monitoring and prediction; to evaluate legacy indicators as well as recent advances in monitoring products, in a case study context; and to discuss cross-cutting issues with indicator construction, performance, and choice.

This work represents an ongoing interest of NOAA's Drought Task Force (DTF; Wood et al. 2015; Hoerling et al. 2014; Schubert et al. 2016), which has extensively discussed and evaluated the merits of drought indicators, especially in the context of compound drought events with strong temperature and precipitation contributions and under emergent conditions such as climate change and increased human management of the water cycle (Zhou et al. 2019a,b). These discussions build on years of DTF science supporting advances in the indicator suite and drought monitoring capabilities and products. The case study framing of this article was proposed by the first DTF (Wood et al. 2015), and has continued to serve as a framework for the second and third DTFs. Case studies provide an opportunity to benchmark the performance of capabilities in a real-world context, testing the ability of different methods and products to function properly in discerning the causes of and conditions in actual drought events, which are highly integrative of multiple forcing factors and stresses in the water cycle.

Scientific background

The term "drought" encompasses a variety of factors related to a dryness anomaly, impacting the soil, the biosphere, agricultural, and/or water resources. The key variable behind droughts is soil moisture. The state of soil moisture is determined by the temporal cumulative (im)

balance between precipitation supply and losses as evapotranspiration and runoff. As such, low soil moisture conditions can result from a negative anomaly in water supply, i.e., precipitation in the form of either snowfall or rainfall, by an anomaly in atmospheric demand due to radiation and increased temperature (Maes et al. 2019) or by a modification of the surface such as land cover or vegetation (Lemordant et al. 2018). This anomaly can be due to anomalous warming and/or atmospheric drying due to atmospheric dynamical patterns, such as synoptic blocking or intense subsidence in the midlatitudes, or to El Niño and its impact on temperature (Bretherton and Sobel 2003) and precipitation in the tropics (Sarachik and Cane 2010). Higher future atmospheric demand due to the combination of increased temperature and atmospheric dryness (Byrne and O'Gorman 2013, 2016; Lemordant and Gentine 2019) will increase atmospheric demand in the future (Grossiord et al. 2020; Ficklin and Novick 2017; Novick et al. 2016; Zhou et al. 2019b), thus potentially decreasing surface soil moisture conditions (Lemordant et al. 2018). In turn, low soil moisture conditions can further increase atmospheric demand as the increased sensible heat flux and lower evaporation rates favor increased vapor pressure deficit (the difference between saturated and actual vapor pressure) (Gentine et al. 2016; Zhou et al. 2019a), generating compound drought and heat wave events (Zhou et al. 2019b).

One challenge in assessing droughts is related to the fact that droughts take on multiple forms and have multiple impacts from reservoir and water resource management to vegetation health, and therefore, many metrics have been defined to assess their impact, with a particular application in mind. These indices may have various degrees of fidelity largely dependent on the data availability.

To understand what regulates drought, it is useful to use a simple water balance model and the Penman–Monteith equation (Penman 1948; Monteith 1965). A bulk water balance model (Gentine et al. 2012; Williams et al. 2020) can be written as

$$nz_r \frac{ds}{dt} = P - \mathrm{ET} - Q,$$

with n the soil porosity, z_r the plant rooting depth or active evaporative depth, s the relative soil moisture, P precipitation, ET evapotranspiration, and Q runoff. Snow could also be accounted for and would mainly generate a lag due to the additional melting process. Clearly, the current water storage depends on the cumulative precipitation minus evapotranspiration (and runoff), i.e., on the history of supply and atmospheric demand.

To better understand the drivers of ET we use the Penman–Monteith equation, which provides the essential physical intuition on ET:

$$\mathrm{ET} = \frac{1}{L_v} \frac{R_n - G + \dfrac{\rho_a c_p}{\Delta} \dfrac{\mathrm{VPD}}{r_a}}{1 + \dfrac{\gamma}{\Delta}\left(1 + \dfrac{r_s}{r_a}\right)},$$

with R_n net radiation, G ground heat flux, L_v the latent heat of vaporization, VPD the vapor pressure deficit, ρ_a the density of the air, c_p the heat capacity of the air, Δ the slope of the Clausius–Clapeyron relationship, γ the psychrometric constant, r_a the aerodynamic resistance related to the turbulent efficiency of the air, and r_s the surface resistance to evapotranspiration, which increases with dryness in the soil and atmosphere (Kennedy et al. 2019; Lu et al. 2020; Medlyn et al. 2011). ET is therefore controlled by changes in the evaporative demand, i.e., available energy ($R_n - G$) and the atmospheric dryness (VPD), but ET is also regulated by water supply affecting r_s. Therefore, a dryness metric should ideally encompass the concepts of water supply and demand as well as soil moisture regulation on surface resistance and therefore on ET. To meet these requirements, empirical indicators have been developed (Dai et al. 2004)

or land surface models resolving the surface energy and water balances have been used (Kennedy et al. 2019; Nie et al. 2019; Graf et al. 2006; Gan et al. 2019).

Indicators for monitoring and predicting droughts

Indicators of droughts have been developed to represent everything from precipitation deficits, evaporative demand increases, soil moisture deficits, and vegetative stress and decline to overall water balance deficits. When applied to drought monitoring, these indicators reflect different facets of drought, and provide the foundational inputs for national drought monitoring efforts such as the U.S. Drought Monitor (Svoboda et al. 2002) or international drought monitoring efforts such as the Famine Early Warning Systems Network (FEWS NET; Funk et al. 2019). In drought prediction, whether on subseasonal to seasonal time scales (Sheffield et al. 2014; Shukla et al. 2014) or climate time scales (Trenberth et al. 2014; Dai et al. 2004; Dai 2011), only a subset of indicators can be computed due to the physical limitations of and available outputs from models. The earliest, and most widely used indicators were developed to require a minimum number of readily available inputs from weather stations, such as precipitation and air temperature. In the last three decades, the advent of land surface models that run routinely for monitoring or forecasting has opened up many more possibilities for calculating drought indicators. Because the availability of data and/or model outputs determines which indicators are possible, we broadly classify indicators into traditional and land surface model based, with a third category—remotely sensed—to be discussed in a later section.

Traditional drought indicators. As noted in the Introduction, dozens of drought indicators are in common use (e.g., Heim 2002; Keyantash and Dracup 2002; Svoboda and Fuchs 2017). These references discuss the full range of indicators in detail, including their advantages and disadvantages. Therefore, we only briefly review the most commonly used indicators below. For convenience, we summarize the indicators discussed in this work in Table 1.

SPI. The standardized precipitation index (SPI) is based on water supply anomalies and requires only precipitation as input (McKee et al. 1993, 1995). SPI quantifies precipitation

Table 1. Drought indicators discussed in this work along with their possible data sources.

Indicator name	Data source
Standardized precipitation index (SPI)	Ground, model, satellite
Standardized precipitation evapotranspiration index (SPEI)	Ground, model, satellite
Palmer drought severity index (PDSI)	Ground, model, satellite
Soil moisture percentiles	Ground, model, satellite
Groundwater percentiles	Ground, model
Standardized runoff index (SRI)	Ground, model
1 April snow water equivalent (SWE)	Ground, model
Severity–area–duration (SAD) analysis	Model, satellite
Vegetation drought response index (VegDRI)	Ground + satellite + model
Quick drought response index (QuickDRI)	Ground + satellite + model
Evaporative demand drought index (EDDI)	Ground, model
Evaporative stress index (ESI)	Satellite
Solar-induced fluorescence (SIF)	Satellite
Vegetation optical depth (VOD)	Satellite
Normalized difference vegetation index (NDVI)	Satellite
Enhanced vegetation index (EVI)	Satellite
Terrestrial water storage percentiles	Satellite + model

anomalies as a standardized departure from a parameterized probability distribution function of historical precipitation, as shown in Fig. 1. As such, it does not take into account the concept of water demand. One key advantage is that it is straightforward to compute SPI as only precipitation data or forecasts are required. The historical precipitation used in the calculation of SPI is typically over a period of 1–24 months, with 12, 6, and 3 months being common. The number of months is often listed with the abbreviation, to denote the period being considered, e.g., 6-month SPI is denoted SPI6, and so forth.

SPEI. The standardized precipitation evapotranspiration index (SPEI; Vicente-Serrano et al. 2010) is a modified version of SPI, trying to address the fact that SPI does not account for changes in atmospheric demand (ET), especially due to temperature variability and extremes. SPEI requires precipitation, temperature, and optionally relative humidity and wind speed as inputs, making it useful for both monitoring and forecasts. SPEI is based on the temporal aggregation of a water balance P – PET, with PET the potential evaporation instead of the actual ET. As such, SPEI will always overestimate the impact of atmospheric demand on droughts as PET > ET. Yet an advantage of SPEI is its simplicity, because it only requires P and T data when computing PET using the Thornthwaite equation (Thornthwaite 1948). When using the Penman–Monteith equation (Allen et al. 1998), additional weather data such as wind speed and relative humidity are required. This aggregated value is then normalized similarly to SPI to define the frequency based on a parameterized distribution (a three-parameter log-logistic distribution).

PDSI. The Palmer drought severity index (PDSI; Palmer 1965) is maybe the most popular drought index and is based on the concept of water supply and demand to estimate soil dryness, and because it requires only precipitation, temperature, and relative humidity as inputs, it is commonly used in both monitoring and forecasting. It is generally computed on a monthly time scale and is adjusted based on local historical conditions as anomalies. As such, PDSI is not only sensitive to water supply deficit, but also to variability in atmospheric demand such as higher vapor pressure deficit. Computing PDSI is more involved than SPI or SPEI, as it requires the computation of a water budget. Similar to SPEI, it has been shown that the computation of PDSI is sensitive to the calculation of PET (e.g., Milly and Dunne 2016).

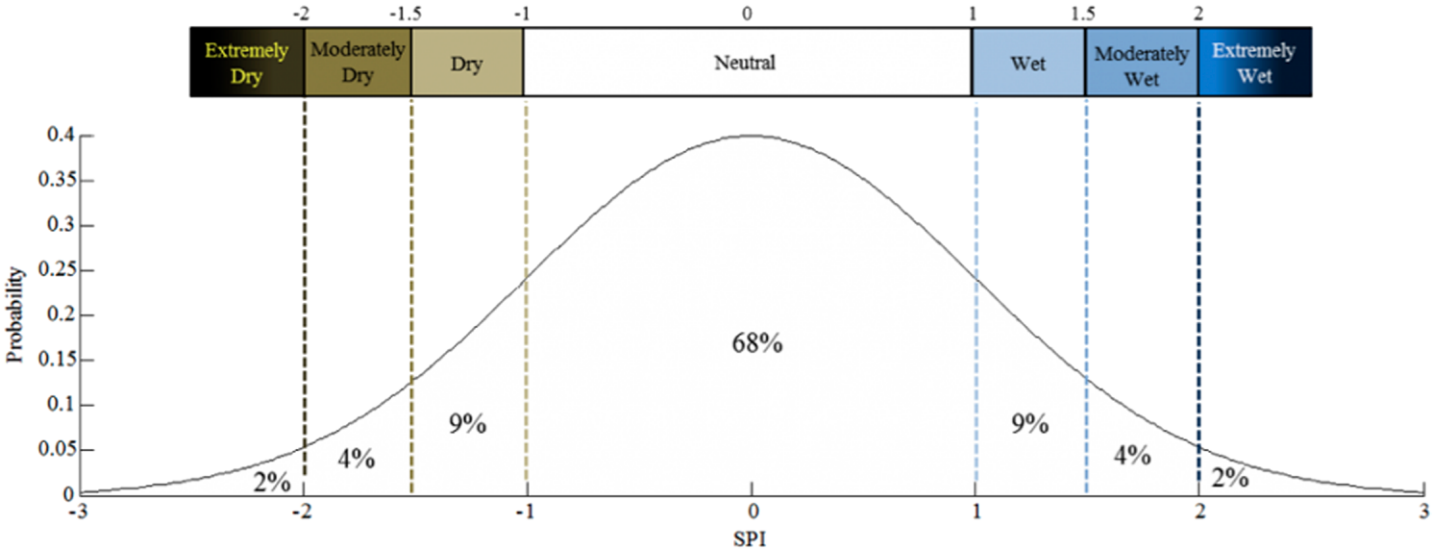

Fig. 1. Probability distribution for the standardized precipitation index (SPI), showing percentiles and relationships to descriptions of moisture deficit and/or surplus conditions. (Figure from https://climatedataguide.ucar.edu/climate-data/standardized-precipitation-index-spi**.)**

Land surface model–based drought indicators. Land surface models are now used on a routine basis for drought monitoring (Mo 2008). For instance, the North American Land Data Assimilation System (NLDAS) (Xia et al. 2012; Mitchell et al. 2004) and Global Land Data Assimilation System (GLDAS) (Rodell et al. 2004) use land surface model (LSM) datasets forced by best-available observations and reanalyses to provide near real time (few days of lag) estimates of various hydrological variables such as total or top 1-m soil moisture, streamflow, evapotranspiration, or snow water equivalent (SWE). The calculation of water and energy budgets in land surface models suggests that approximate methods such as PDSI may in the future be superseded by land surface model–based water budgets, Further, because land surface models in systems such as NLDAS are run continuously on a regular grid, they are more amenable than point-based networks to drought characterization at regional scales. Percentiles (calculated relative to the long-term climatology of the LDAS, for each point and time of year) and anomalies of those variables can then be used to define the level of droughts. Yet these models include a myriad of parameters that ideally would be regionally tuned, leading to difficulties in their specification and uncertainties in their output. We discuss some commonly used land surface model–based drought indicators below.

Soil moisture percentiles. Land surface models provide spatially and temporally continuous soil moisture estimates at multiple depths that are especially useful for monitoring agricultural drought (Mo 2008; Mo et al. 2011). The NLDAS experimental drought monitor routinely provides soil moisture percentiles, which can be related to the U.S. Drought Monitor using similar definitions of drought occurrence and severity (e.g., 20th percentile as threshold for drought) as well as an optimal weighting scheme (Xia et al. 2014a,b). Model-based reconstructions of soil moisture have been applied to studies of flash drought (Mo and Lettenmaier 2015, 2016), historical drought trends (Mo and Lettenmaier 2018) and drought projections (Cook et al. 2015; Williams et al. 2020).

SRI. The standardized runoff index (SRI) is used to classify hydrological droughts (Shukla and Wood 2008) using model-based runoff. Similar to the SPI, the aggregation period may be 1 month or more.

1 April SWE. SWE is a key indicator of water availability in snowpack. Snowpack and related snowmelt are crucial for water resources in most Northern Hemisphere regions (Barnett et al. 2005); 1 April SWE is a standard indicator of water supply in the western United States, because on this date snowpack is typically at its maximum value; 1 April SWE has been used as an indicator of snow drought by several authors (Mao et al. 2015; Cooper et al. 2016; Dierauer et al. 2019).

SAD analysis. While not technically a different type of indicator, droughts can be characterized by three distinct indicators for severity, duration, and areal extent. By replacing storm depth with a measure of drought severity, severity–area–duration (SAD) curves can be constructed in an analog to precipitation depth–area–duration analysis. This approach has been used to evaluate twentieth century droughts in the United States (Andreadis et al. 2005), and is a useful way to summarize multiple dimensions of drought.

Satellite remote sensing capacities and indicators

Over the years, there have been tremendous advances in observational capacities of precipitation and drought conditions using satellite remote sensing. AghaKouchak et al. (2015) provide a review of remote sensing of drought, including current and emerging monitoring approaches. These capacities have added to our ability to diagnose and monitor conditions,

particularly in areas with limited in situ precipitation gauges and other direct measurements. Many of these retrievals also offer the opportunity to provide early warning of water stressed conditions. The observational capacities take advantage of signals in various wavelengths, including microwave, infrared, visible, and thermal, in addition to changes in the gravity field.

Precipitation. Retrievals from the Tropical Rainfall Measuring Mission (TRMM; Simpson et al. 1988; Kummerow et al. 2000), from the Global Precipitation Measurement (GPM; Hou et al. 2014) mission, and numerous other satellites have led to the development of precipitation products such as TRMM Multisatellite Precipitation Analysis (TMPA; Huffman et al. 2007), Integrated Multisatellite Retrievals for GPM (IMERG; Huffman et al. 2015; Tan et al. 2019), Global Precipitation Climatology Project (GPCP; Huffman et al. 1997), Climate Hazards Group Infrared Precipitation with Station data (CHIRPS; Funk et al. 2015), Climate Prediction Center morphing technique (CMORPH; Joyce et al. 2004; Joyce and Xie 2011), and Precipitation Estimation from Remotely Sensed Information Using Artificial Neural Networks (PERSIANN; Hsu et al. 1997). These products have led to improved understanding and climatologies of historical precipitation as well as better real-time global/regional monitoring. For example, CHIRPS is routinely used by FEWS NET to calculate SPI over its period of record (Funk et al. 2019).

Soil moisture. Soil moisture measurements are crucial for diagnosing agricultural drought. The number of in situ measurement sites continues to expand, including mesonets, and networks such as the U.S. Department of Agriculture, Natural Resources Conversation Service's (USDA/NCRS's) snow telemetry sites (SNOTEL; Serreze et al. 1999) and Soil Climate Analysis Network (SCAN; Schaefer et al. 2007), and NOAA's U.S. Climate Reference Network (USCRN; (Diamond et al. 2013). These and other networks have been standardized into products such as the (U.S.) National Soil Moisture Network (http://nationalsoilmoisture.com/; Quiring et al. 2016) and the International Soil Moisture Network (ISMN; Dorigo et al. 2011). However, these networks are still too limited to provide a spatially and temporally consistent dataset. Microwave remote sensing has expanded soil moisture measurements to provide global coverage and consistent measurements for the first time. Missions such as the European Space Agency's Soil Moisture Ocean Salinity (SMOS; Kerr et al. 2001) and NASA's Soil Moisture Active Passive (SMAP; Entekhabi et al. 2010) have provided microwave-based retrievals of surface soil moisture. The SMAP level 4 product (Reichle et al. 2019) combines the SMAP surface retrievals with an LSM through data assimilation to provide root zone soil moisture products. Satellite remote sensing-based soil moisture can be used for drought analysis, offering new views on the spatial and temporal behavior of droughts (e.g., (Nicolai-Shaw et al. 2017).

Vegetation indices. Visible imagery is widely used to monitor drought conditions from satellite. Visible and near-infrared wavelengths are used to monitor vegetation greenness, an indicator of vegetation productivity. Healthy vegetation reflects more near-infrared and green light and absorbs more red and blue light compared to other wavelengths. This has been used to generate indices measuring the difference between reflected near-infrared and absorbed red light, such as the normalized difference vegetation index (NDVI; Tucker 1979). Droughts impact vegetation health so that NDVI is directly connected to water stress. However, other biotic and abiotic factors also impact vegetation health and thus NDVI, leading to potentially confounding factors. Alternatives to NDVI include 1) normalized difference water index (NDWI; Gao 1996), which is an improvement over NDVI and tends to saturate less in high biomass environments, but is still sensitive to the soil background; and 2) enhanced vegetation index (EVI; Jiang et al. 2008), which is a modified version of NDVI aiming at correcting its lack of

sensitivity in high biomass regions and reducing the background signal pollution (soil and atmosphere); or 3) more objective versions of those empirical indices using machine learning such as the contiguous solar induced fluorescence (CSIF; Zhang et al. 2018b). These vegetation retrievals have been used as input to various drought indices, such as the vegetation drought response index (VegDRI; Brown et al. 2008). Vegetation retrievals are also used as input parameters to land surface models in LDASs.

Thermal evaporative stress. Thermal imagery is also adding value to drought monitoring and detection. Land surface temperatures (LST) retrieved from thermal remote sensing can be used to estimate evapotranspiration, including vegetation stress, as the latent heat flux is the most efficient cooling mechanism in warm conditions (Bateni and Entekhabi 2012). For instance, the evaporative stress index (ESI; Anderson et al. 2007, 2011) uses inputs of LST and leaf area index (LAI), and takes advantage of the high temporal resolution of measurements from geostationary satellites. Evaporative stress has been shown to perform well in monitoring rapidly changing or "flash" droughts (Otkin et al. 2013), often earlier than other more traditional drought products and indices. The ESI performs well due to its high temporal resolution that is able to detect areas with rapid increases in drought stress, and can provide an early warning of a risk of drought intensification (Otkin et al. 2014).

Solar-induced fluorescence. In recent years, solar-induced fluorescence (SIF) has been shown to be detectable using existing satellite missions, starting with *Greenhouse Gas Observing Satellite* (*GOSAT*; Joiner et al. 2012; Köhler et al. 2015), Global Ozone Monitoring Experiment 2 (GOME-2; Bacour et al. 2019; Joiner et al. 2013; He et al. 2017), *Orbiting Carbon Observatory 2* (*OCO-2*; Sun et al. 2017; Yu et al. 2019) and now with Tropospheric Monitoring Instrument (TROPOMI; Doughty et al. 2019). SIF is a flux that is a direct proxy for photosynthesis (Li et al. 2018; Xiao et al. 2019), especially at relatively coarse spatial (few kilometers) and temporal scales (weeks) (Sun et al. 2017). Since SIF is a flux more directly connected to vegetation productivity, it provides a unique estimate of vegetation water stress (Sun et al. 2017; Pagán et al. 2019; Hamed Alemohammad et al. 2017). As such it has been used to assess the role of droughts or heat waves on ecosystem productivity (Helm et al. 2020; Wang et al. 2019; Sun et al. 2015; Zhang et al. 2018a), showing a potential even in cases where soil moisture would not necessarily be appropriate.

Vegetation optical depth. Vegetation optical depth (VOD) is another relatively recent remote sensing product related to vegetation productivity (Vaglio Laurin et al. 2020; Zhou et al. 2018; Li et al. 2013; Li et al. 2015; Liu et al. 2011; Rodríguez-Fernández et al. 2018; Piles et al. 2017; Wild et al. 2020) based on passive microwave remote sensing. VOD is related to above ground vegetation water content, itself proportional to dry biomass (the dominant factor) and plant tissue relative water content (Konings and Momen 2018; Zhang et al. 2019). VOD directly connects to vegetation hydraulics and thus water stress (Konings and Gentine 2017; Novick et al. 2019; Konings et al. 2017; Giardina et al. 2018), offering a complementary information to that obtained from soil moisture or SIF.

Terrestrial water storage. Gravity measurements can also be used to monitor water storage changes. The Gravity Recovery and Climate Experiment (GRACE) twin satellites are used to calculate monthly terrestrial water storage (TWS) anomalies, with negative anomalies representing total column-integrated water deficit (e.g., Rodell 2012; Thomas et al. 2014), over large spatial extents (hundreds of kilometers). GRACE TWS anomalies have also been assimilated into LSMs/LDASs for drought monitoring (Houborg et al. 2012; Kumar et al. 2016; Girotto et al. 2016; Li et al. 2019) as shown at http://nasagrace.unl.edu.

Model-based reconstruction of CONUS droughts

Land surface models vary in terms of their complexity and representation of physical processes. For instance, recent land surface models have the option to choose between a dynamic or static climatological phenology, which can further modify the ET response through changes in both the surface roughness (and related aerodynamic resistance, see Penman–Monteith equation) and surface resistance, or can include a groundwater scheme (typically a water table) (Nie et al. 2019; Gan et al. 2019). As an illustrative example, the community Noah-MP LSM, a medium-complexity energy and water balance model, uses multiple options for key land–atmosphere interaction processes (Niu et al. 2011; Yang et al. 2011). Two of these physics options are particularly relevant for drought applications: groundwater and dynamic phenology. There are several schemes available in Noah-MP for surface water infiltration and runoff, and groundwater transfer and storage, including water table depth to an unconfined aquifer (Niu et al. 2007). The Noah-MP model can be executed by prescribing both the horizontal and vertical density of vegetation using either ground- or satellite-based observations. Another available option is for prognostic vegetation growth that combines a Ball–Berry photosynthesis-based stomatal resistance with a dynamic phenology model (Dickinson et al. 1998) that allocates carbon to various parts of vegetation (leaf, stem, wood, and root) and soil carbon pools (fast and slow).

Forcing extension. To illustrate the physics impacts, the Noah-MP LSM was used to reconstruct CONUS droughts for the period 1915–2018. Atmospheric forcing data consisted of daily precipitation P, wind speed, and daily maximum and minimum temperature (Tmax and Tmin). This forcing data at 1/16° spatial resolution for years 1915–2011 were taken from the Livneh et al. (2013) dataset and extended through 2018 using the same methods. A forcing evaluation was conducted, which showed that the extended forcing is consistent with the original dataset (figures not shown) in an overlap period (1961–2011). After the forcing data were extended, they were aggregated to 1/8° to be consistent with NLDAS. Additional required atmospheric forcing data (downward shortwave and longwave radiation, and vapor pressure) were then estimated following methods summarized by Bohn et al. (2013). The reader is referred to Su et al. (2021) for details.

Baseline CONUS drought reconstruction. Three different runs were performed using Noah-MP: 1) a baseline (BASE) run using the "standard" Noah-MP setup (Su et al. 2021), 2) a run (DYNAVEG) with the dynamic vegetation phenology option implemented (Dickinson et al. 1998), and 3) a run (GW) with a Noah-MP groundwater option (Niu et al. 2007). Using the BASE output of total column soil moisture (SM) (aggregated over all four Noah-MP layers), percentiles were calculated relative to that month's and that grid cell's 1916–2017 history. (Note: The first and last years of the reconstruction are removed due to a 5-day window for percentile calculations.) Drought events were defined as having SM percentiles below a threshold (20%) that is equivalent to the U.S. Drought Monitor (Svoboda et al. 2002) D1 threshold. Drought durations were also required to exceed five months. Events were selected in which the average drought area exceeded the 90th percentile for the 1916–2017 period (>38% of entire CONUS domain). There were 10 such events in BASE, which are listed in Table 2. Superscripts denote events that occurred only when physics options were varied relative to BASE. The 10 identified events are fewer than results in Mo and Lettenmaier (2018), who conducted a similar analysis, since our threshold (20%) was more stringent than theirs (30%). Figure 2 shows the average SM percentiles for 4 of the 10 events. As shown in Table 2, all 10 of the events covered at least 38% of CONUS (averaged over their durations). The longest of the events (July 1954–May 1955) lasted 11 months. The greatest area covered (52%) was for the May 1934–November 1934 event, which was shorter (7 months) than most of the other events. The December 1976–August 1977 event was among the top three severe droughts in terms of both duration

and spatial coverage. While the 2012 event was the most widespread of the past 40 years, its spatial coverage was less than that of the other events over the longer 100-yr period of record considered in this reconstruction. This helps underscore the value of extended reconstruction for examining extreme events such as droughts.

Table 2. The duration, coverage, and severity of the great drought events. These are a union of events classified based on BASE, DYNAVEG, and GW SM outputs, and with different drought indices (SPI, SPEI, PDSI). Events classified in all three configurations are listed without superscripts; events classified using drought indices but not in BASE are listed with an asterisk (*); events classified both in DYNAVEG/GW and using drought indices but not in BASE are listed with two asterisks (**). All values given are from the BASE run.

Events	Peak coverage date	Duration (month)	Average coverage (%)	Peak coverage	Minimum coverage	Average severity	Peak severity	Minimum severity	Peak severity date
December 1917–April 1918	January 1918	5	46	55	42	8.0	6.8	9.5	April 1918
April–September 1925**	June 1925	6	41	48	35	8.5	8.0	8.9	September 1925
May–November 1931	July 1931	7	41	47	37	8.9	8.0	9.9	June 1931
May–November 1934	August 1934	7	52	60	42	7.7	6.4	8.7	June 1934
June–September 1936	July 1936	7	45	51	36	7.2	5.9	8.1	August 1936
October 1939–April 1940	January 1940	7	45	53	36	8.7	7.7	9.4	April 1940
October 1953–April 1954	November 1953	7	42	50	36	8.2	7.6	9.2	December 1953
July 1954–May 1955	August 1954	11	41	45	36	8.5	7.4	9.1	October 1954
September 1956–March 1957	December 1956	7	48	53	40	7.6	6.8	8.2	October 1956
November 1963–April 1964**	November 1963	6	36	43	33	9.1	8.2	10.1	November 1963
December 1976–August 1977	February 1977	9	47	54	38	7.5	6.2	9.1	February 1977
September 1980–January 1981*	January 1981	5	23	32	16	10.7	10.0	11.6	September 1980
November 1999–September 2000*	February 2000	11	25	35	15	10.7	9.4	12.2	March 2000
July–December 2012	July 2012	6	38	42	34	9.5	8.9	10.1	August 2012

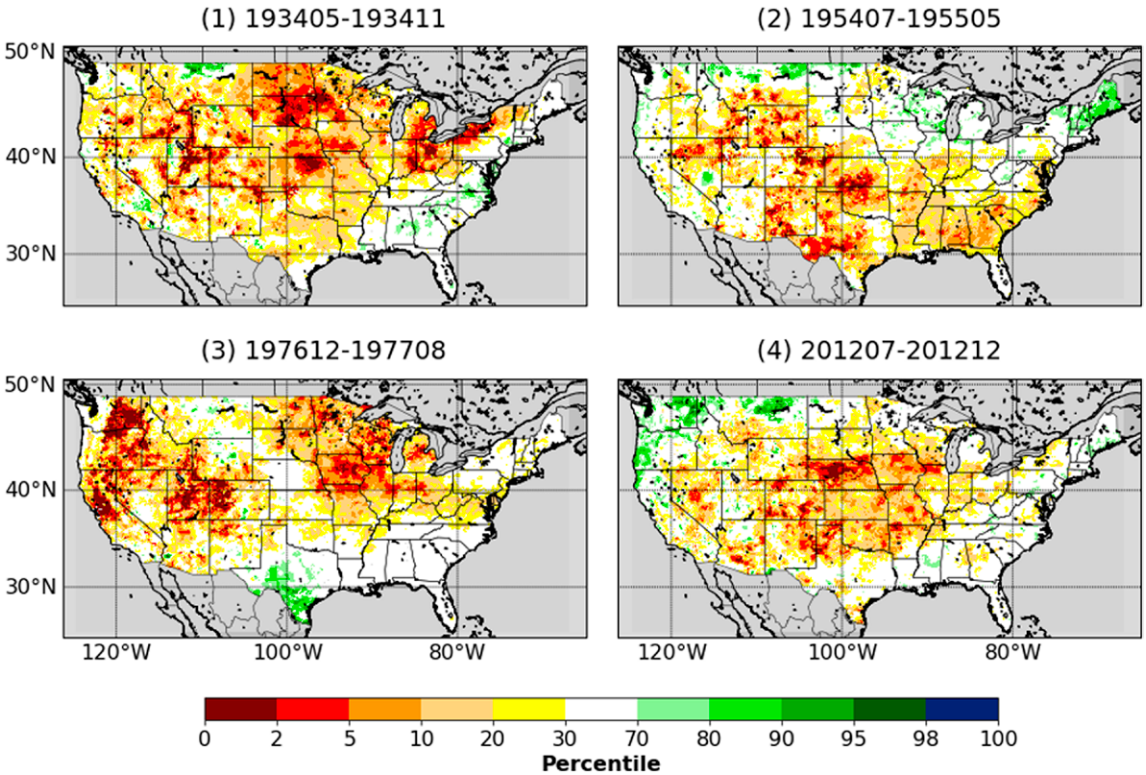

Fig. 2. SM percentiles in BASE averaged over the duration of four representative events: May–November 1934, July 1954–May 1955, December 1976–August 1977, and July–December 2012.

Comparison of soil moisture percentiles to other drought indicators. The events listed in Table 2 were also classified using the 20th percentile threshold of the 6-month standardized precipitation index (SPI6), the 6-month standardized precipitation evapotranspiration index (SPEI6), and the PDSI. We used two methods to compute PET (required by SPEI and PDSI) to avoid complications with temperature-based PET methods such as Thornthwaite (1948). As noted by Sheffield et al. (2012) evapotranspiration is a function of more than just temperature, and the correct physics includes radiative and aerodynamic controls on evaporative demand, as well as surface water stress regulation on supply. In this respect, the Penman–Monteith (PM) equation (Penman 1948; Monteith 1965) applied for a reference crop (typically short grass, denoted ET0) arguably is a better choice as a surrogate for PET. For this purpose, we implemented PM ET0 following Allen et al. (1998); however, we also report the previous results for the more common Thornthwaite method (which we denote TH). We note that ET0 does not include the soil moisture and vapor pressure deficit stressors on the surface resistance, which can be important especially under droughts (Gentine et al. 2019; Massmann et al. 2019). We show results for SPEI and PDSI based on both TH and PM methods (denoted as SPEI_TH, SPEI_PM, PDSI_TH, PDSI_PM, respectively) in addition to SPI and SM percentiles in BASE, GW, and DYVEG.

Figure 3 shows the spatially averaged SM percentile of the Noah-MP variants (BASE, GW, and DYNAVEG) in the left panels, while the right panels show the different drought indicators from the BASE simulation, including the SM percentile again, in the right panels. The spatial extent for each event was determined where the pixels

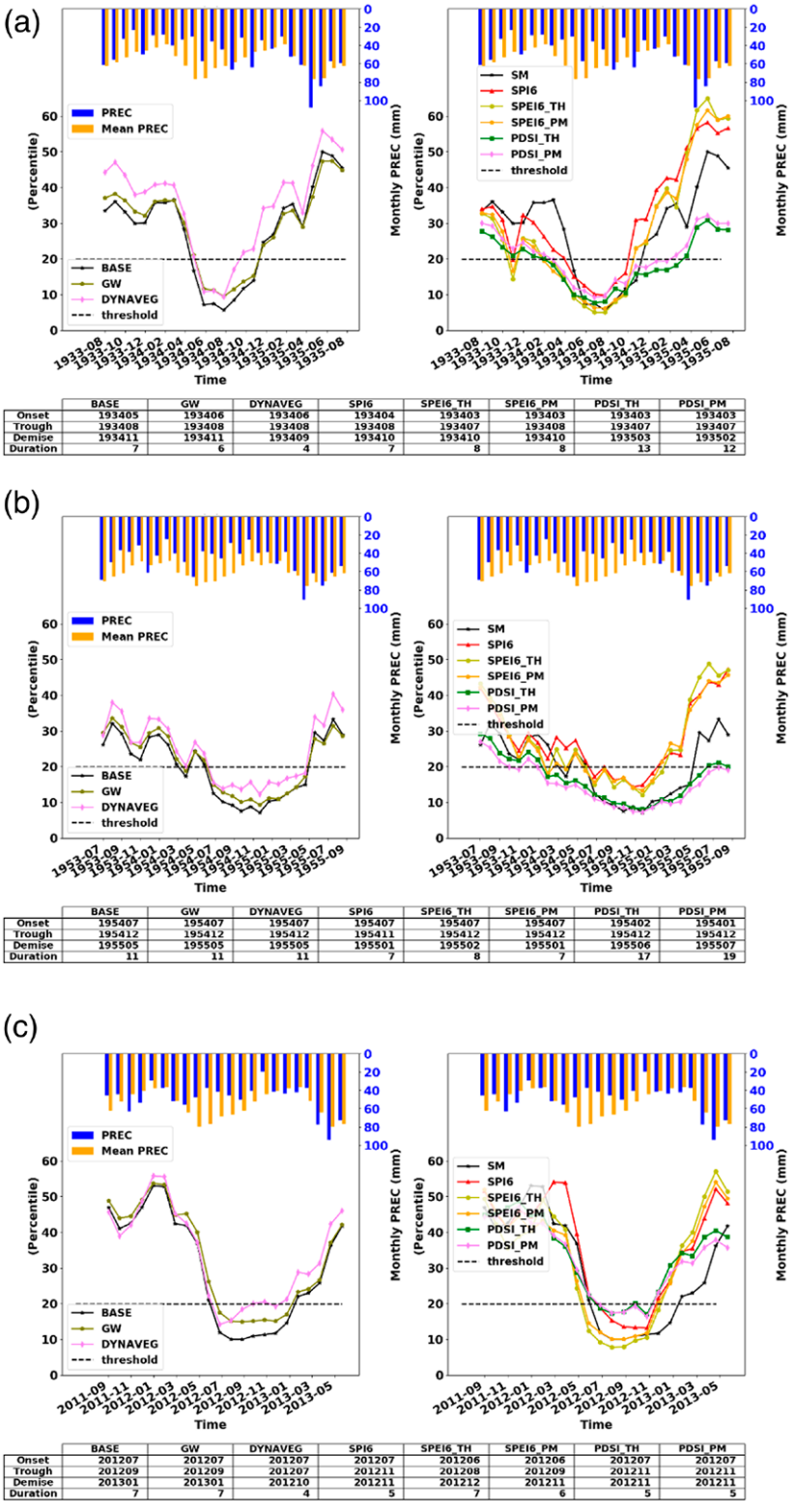

	BASE	GW	DYNAVEG	SPI6	SPEI6_TH	SPEI6_PM	PDSI_TH	PDSI_PM
Onset	193405	193406	193406	193404	193403	193403	193403	193403
Trough	193408	193408	193408	193408	193407	193408	193407	193407
Demise	193411	193411	193409	193410	193410	193410	193503	193502
Duration	7	6	4	7	8	8	13	12

	BASE	GW	DYNAVEG	SPI6	SPEI6_TH	SPEI6_PM	PDSI_TH	PDSI_PM
Onset	195407	195407	195407	195407	195407	195407	195402	195401
Trough	195412	195412	195412	195411	195412	195412	195412	195412
Demise	195505	195505	195505	195501	195502	195501	195506	195507
Duration	11	11	11	7	8	7	17	19

	BASE	GW	DYNAVEG	SPI6	SPEI6_TH	SPEI6_PM	PDSI_TH	PDSI_PM
Onset	201207	201207	201207	201207	201206	201206	201207	201207
Trough	201209	201209	201207	201211	201208	201209	201211	201211
Demise	201301	201301	201210	201211	201212	201211	201211	201211
Duration	7	7	4	5	7	6	5	5

Fig. 3. Spatially averaged SM percentiles (over extent of drought estimated using BASE) for (left) other Noah-MP variants and (right) other drought indicators (expressed as percentiles) for the droughts of (a) 1934, (b) 1954, and (c) 2012. Bars at the top are actual (blue) and climatological (orange) monthly precipitation during the drought period, averaged over the drought extent.

have the mean BASE percentiles lower than 20% in that event. Spatially averaged percentiles were examined for all the classified events, and here three representative cases (1934, 1954, 2012) are shown. In the left panels, SM percentiles from the BASE run generally produce the lowest values during the most severe drought months, with GW and DYNAVEG somewhat higher. We believe this is related to negative feedbacks on soil moisture drying when GW and DYNAVEG are enabled. Also, DYNAVEG tends to have shorter drought durations. The right panels in Fig. 3 show somewhat different characteristics from those identified using SM. (All SPI, SPEI, and PDSI values are relative to the base period 1951–2010). For the 1934 and 1954 droughts, we see a more or less concurrent drought troughs for different drought indices and SM percentiles (BASE, GW, and DYNAVEG); while for the 2012 event, the drought trough is more spread out. SPI6 and SPEI6 (both SPEI_TH and SPEI_PM) show more similar drought temporal signatures. SPI measures drought conditions only from a precipitation anomaly angle. SPI does not consider evapotranspiration, which may be the reason that SPI generally has the smallest spatially averaged severity (highest percentile) in all three droughts. By standardizing the difference between PET and precipitation, SPEI generally shows a higher severity than (or at least the same as) SPI. PDSI is based on the climatic water balance principle, which also considers the available water holding capacity. Our results show that PDSI (both PDSI_TH and PDSI_PM) has the earliest drought onset, the latest drought termination and thus the longest duration for the 1934 and 1954 events. The construction of PDSI (self-calibrated) produces strong lagged autocorrelations; as a result, the prior soil and climatic conditions have a long-term impact on this index, and this explains at least in part the longer PDSI-based drought durations compared with SPEI6 (Guttman 1998; Zhao et al. 2017). Furthermore, the long-term memory of previous climatic conditions also makes PDSI-based drought recovery slower, and hence later drought termination as compared with the other indices. These results highlight how accounting for separate atmospheric demand terms (such as temperature) in the different indices produce different estimates of the onset, peak, and duration of individual drought events.

The 2012 drought event depicted in Figs. 3e and 3f is further analyzed using a satellite remote sensing drought indicator. The thermal-based ESI is used to compare the onset and demise timing of the 2012 drought as compared to the model-based indices. One challenge in this comparison is that satellite data records are short compared to the 100+ year model simulation period from Noah-MP. We used the ESI, which is only available for the MODIS period (2000 and later). Following the methodology used in Anderson et al. (2011), we performed temporal compositing of the daily ESI data from 2000 to 2018 to a monthly scale to reduce missing pixels due to the presence of clouds as well as reduce the effects of noise in the retrievals. Next, we calculated a pseudo z score to obtain the standardized anomalies over this period. Shown in Fig. 4 is the ESI z score over the same spatial extent of the 2012 drought as used for the time series shown in Figs. 3e and 3f. The ESI anomaly is shown to go rapidly from near-neutral conditions in April 2020 to very low by June 2020. The low value indicates high levels of vegetation stress as retrieved from satellite. Given the different climatologies and comparing a z score to percentiles, the onset and demise months from the curves in Figs. 3e and 3f are depicted as horizonal bars on Fig. 4. The ESI z score leads most of the model-based drought indices by one month, with the notable exception of the SPEI calculations, which also include anomalies in evaporation. This result shows the general consistency of a satellite remote sensing-based drought index, while also showing the potential to capture rapidly emerging drought conditions based on stress with lead time as compared to some other indices.

Dry area coverage trend analysis. We examined trends in dry area coverage over the entire CONUS for 1915–2018 (Table 3) using the different drought indices described above

(including alternate PM-based PET for SPEI and PDSI) using the Mann–Kendall statistical test (Mann 1945; Kendall 1975) and the Theil–Sen slope estimator. We performed trend analyses not only for our entire period of record (1915–2018) but also for 1970–2018 (Table 4). We found that the CONUS dry area fractions with all drought indices except SPEI6_TH show decreasing trends with Theil–Sen slopes in the range from about −0.03 to −0.06 (100 yr)$^{-1}$ (statistically significant at $\alpha = 0.05$) becoming wetter over CONUS over the past 60 years. Dai et al. (2004) found that PDSI_TH showed a drying trend over the period 1900–1949 and a wetting trend over the period 1950–2002 over CONUS. Dai (2013) shows a wetting trend over most of CONUS for 1950–2010 as well as 1923–2010 using PDSI_PM from observational forcings. In general, century-long downtrends in drought (for most drought characteristics) are attributable to dry decades (especially 1930s, but also 1950s) early in the record. We find that for the more recent period beginning in 1970 (not studied by Andreadis and Lettenmaier) that the trend toward decreasing dryness, at least on a CONUS-wide basis, has disappeared. We note though that PDSI only uses an approximation for ET based on unstressed surface resistance. The feedback of soil moisture and increased vapor pressure deficit could alter those trends, but unfortunately, we do not have access to widespread and long-term measurements of ET, even with eddy-covariance towers, which have gaps, too short records, or are too sporadic.

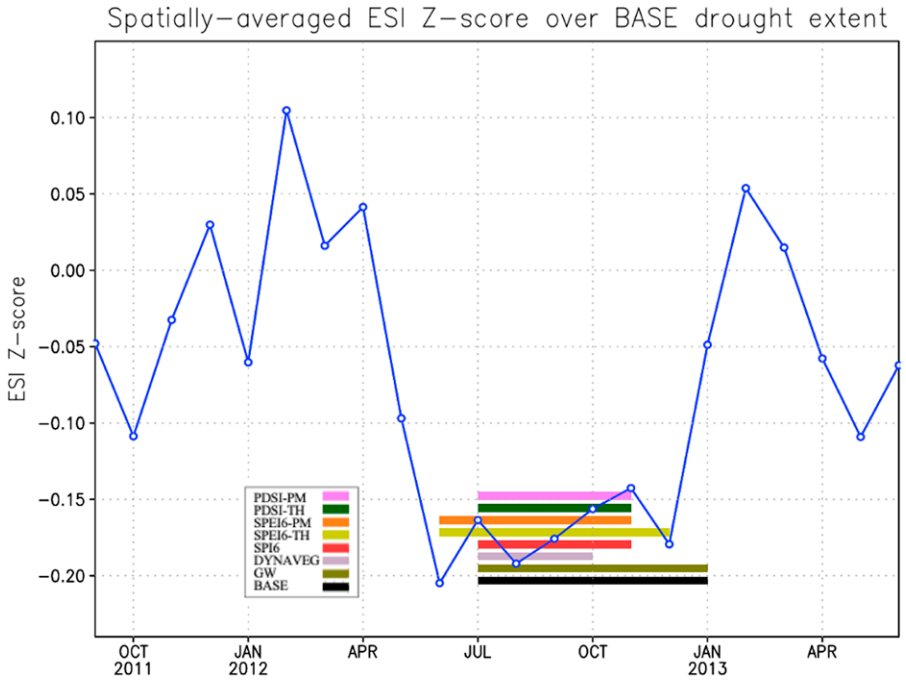

Fig. 4. The *z*-score standardized anomalies of the evaporative stress index (ESI) over the extent of the 2012 drought from the Noah-MP BASE simulation. The blue line (circles) depicts the ESI *z* score for each month from late 2011 to mid 2013. The horizontal bars indicate onset and demise months from the model-based indices as shown in Figs. 3e–f (from bottom to top): BASE (black), GW (olive), DYNAVEG (light violet) and indicators (from top to bottom) PDSI-PM (pink), PDSI-TH (green), SPEI6-PM (orange), SPEI6-TH (gold), SPI6 (red).

Table 3. Trend analysis for CONUS dry area coverage (1915–2018).

	BASE	GW	DYVEG	SPI	SPEI6_TH	SPEI6_PM	PDSI_TH	PDSI_PM
Trend	↓	↓	↓	↓	—	↓	↓	↓
Slope (100 yr)$^{-1}$	−0.06	−0.05	−0.05	−0.06	−0.02	−0.04	−0.04	−0.06
p	2.0×10^{11}	3.4×10^{9}	3.6×10^{9}	1.7×10^{9}	0.13	1.9×10^{4}	4.6×10^{14}	1.0×10^{14}

Table 4. Trend analysis for CONUS dry area coverage (1970–2018).

	BASE	GW	DYVEG	SPI	SPEI6_TH	SPEI6_PM	PDSI_TH	PDSI_PM
Trend	↑	–	↑	—	↑	—	↑	↑
Slope (100 yr)$^{-1}$	0.06	0.02	0.05	−0.02	0.15	0.05	0.08	0.03
p	0.02	0.27	0.02	0.56	1.7×10^{7}	0.10	1.1×10^{8}	0.02

Impact of model physics. The BASE results were compared to the DYNAVEG and GW results using the same drought classification and analysis approach. For the GW run, the percentiles were calculated using the sum of moisture in the soil column and groundwater. Most of the drought events in GW and DYNAVEG also appear in BASE, except two (April–September 1925, November 1963–April 1964) listed in Table 2 with a superscript. Below, we discuss the impact of these physics changes in more detail.

Dynamic vegetation phenology. Compared with BASE, the spatial coverage of events listed in Table 2 for the DYNAVEG reconstruction tend to have smaller spatial coverage by 1%–6% of the CONUS. This suggests that the Noah-MP dynamic phenology scheme feeds back to reduce the drought area relative to the BASE. However, this may be due to an overestimate of stress that effectively shuts down transpiration before the soil moisture storage can be depleted. Similar to the BASE reconstruction discussed here, the majority of operational LSM drought products (such as NLDAS) use a monthly climatology of vegetation parameters, such as the fraction of green vegetation or the LAI. Thus, the LSMs in these systems have the same vegetation characteristics every year, which does not reflect the actual real-world conditions of vegetation senescence during drought and warm conditions (Zhou et al. 2019a). During a drought, an LSM specifying vegetation phenology in this manner will overestimate evapotranspiration, assuming the specified vegetation greenness and leaf area are higher than that during drought stress. New physics options in more advanced LSMs account for these types of processes through dynamic phenology schemes, which grow and shrink leaf biomass. In addition to Noah-MP, other LSMs with this option include the Community Land Model (CLM; Lawrence et al. 2019), Interaction Soil–Biosphere–Atmosphere (ISBA-A-gs; Calvet et al. 2004; Sabater et al. 2008; Barbu et al. 2011), and the Joint U.K. Land Environment Simulator (JULES; Best et al. 2011; Clark et al. 2011). An LSM with a dynamic phenology scheme will also allow for data assimilation of remotely sensed vegetation, to include observations of vegetation health in the LSM to account for vegetation stress during a drought. Because the response of the vegetation to stress is not well constrained in these models, Mocko et al. (2021) assimilated satellite-based LAI into the dynamic phenology scheme of Noah-MP, and showed that assimilation improved the rank correlation of drought categories diagnosed from the LSM improved as compared to the USDM drought categories over the 2000–17 period (Fig. 5). These improvements were most notable in agricultural regions. Other physics improvements, such as a dynamic root system and plant water storage, have been made to the dynamic phenology schemes and have shown benefits in drought applications (e.g., Niu et al. 2020).

Groundwater. While it is not evident for the three droughts shown in Fig. 3, Su et al. (2021) perform a more detailed analysis of the most severe droughts of the record and find some evidence that the model with GW predicts slower recovery than without. This is consistent with the literature suggesting that groundwater anomalies typically lag and integrate precipitation anomalies, and recovery also tends to be lagged behind surface and soil moisture drought recovery (e.g., Wang et al. 2016; Uddameri et al. 2019; Ojha et al. 2020; Hellwig et al. 2021). Groundwater deficits can also contribute to more rapid drought reemergence following short-lived drought recovery, as the memory of the deeper storages can affect agricultural drought, if there is a small deficit of precipitation after the recovery. Well level/height measurements have historically been used for drought monitoring, but GRACE retrievals now support detecting changes and anomalies of groundwater (Houborg et al. 2012). LSMs have also added advanced physics including groundwater (Niu et al. 2011; Lawrence et al. 2019). The GW reconstruction shown in Table 2 and Fig. 3 demonstrates the impact of physics on the most severe historical U.S. droughts. Another example of including groundwater anomalies in drought monitoring is depicted in Fig. 6. The top row shows USDM, and Noah-MP top

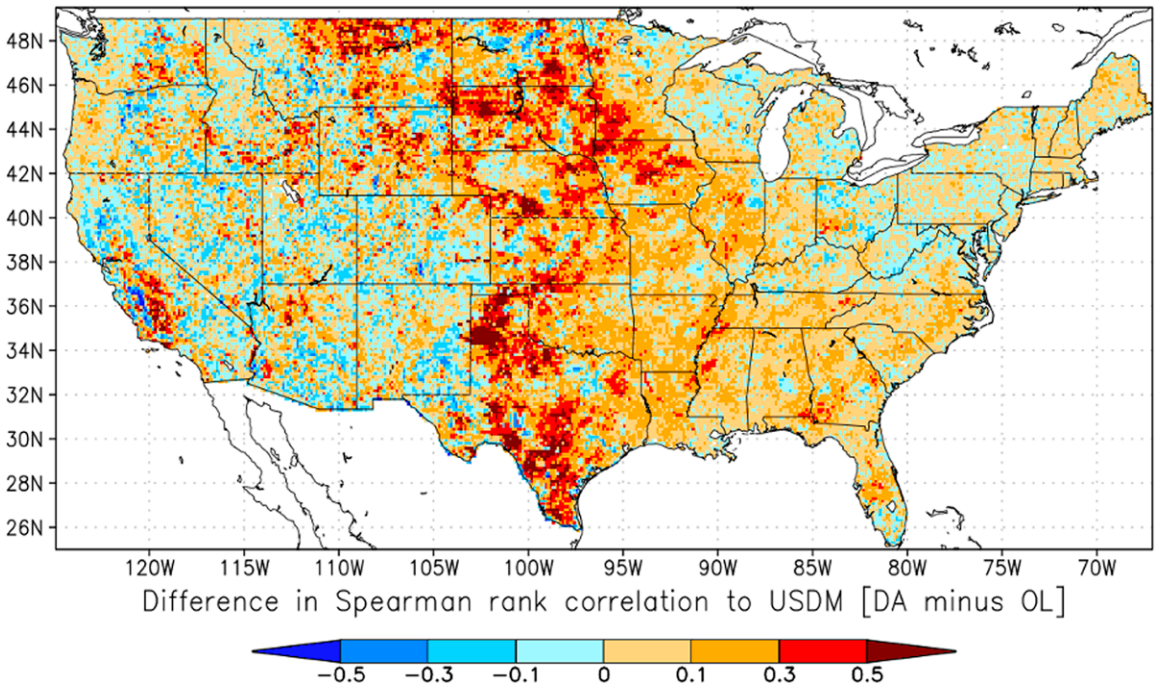

Fig. 5. From Mocko et al. (2021). Difference in Spearman's rank correlation to USDM between the Noah-MP simulation with data assimilation of LAI minus the simulation with no data assimilation. Warm (red) colors indicate locations where the correlation of simulated top 1-m soil moisture drought categories to the USDM improved due to data assimilation of the LAI; cool (blue) colors indicate where LAI data assimilation degraded the correlation.

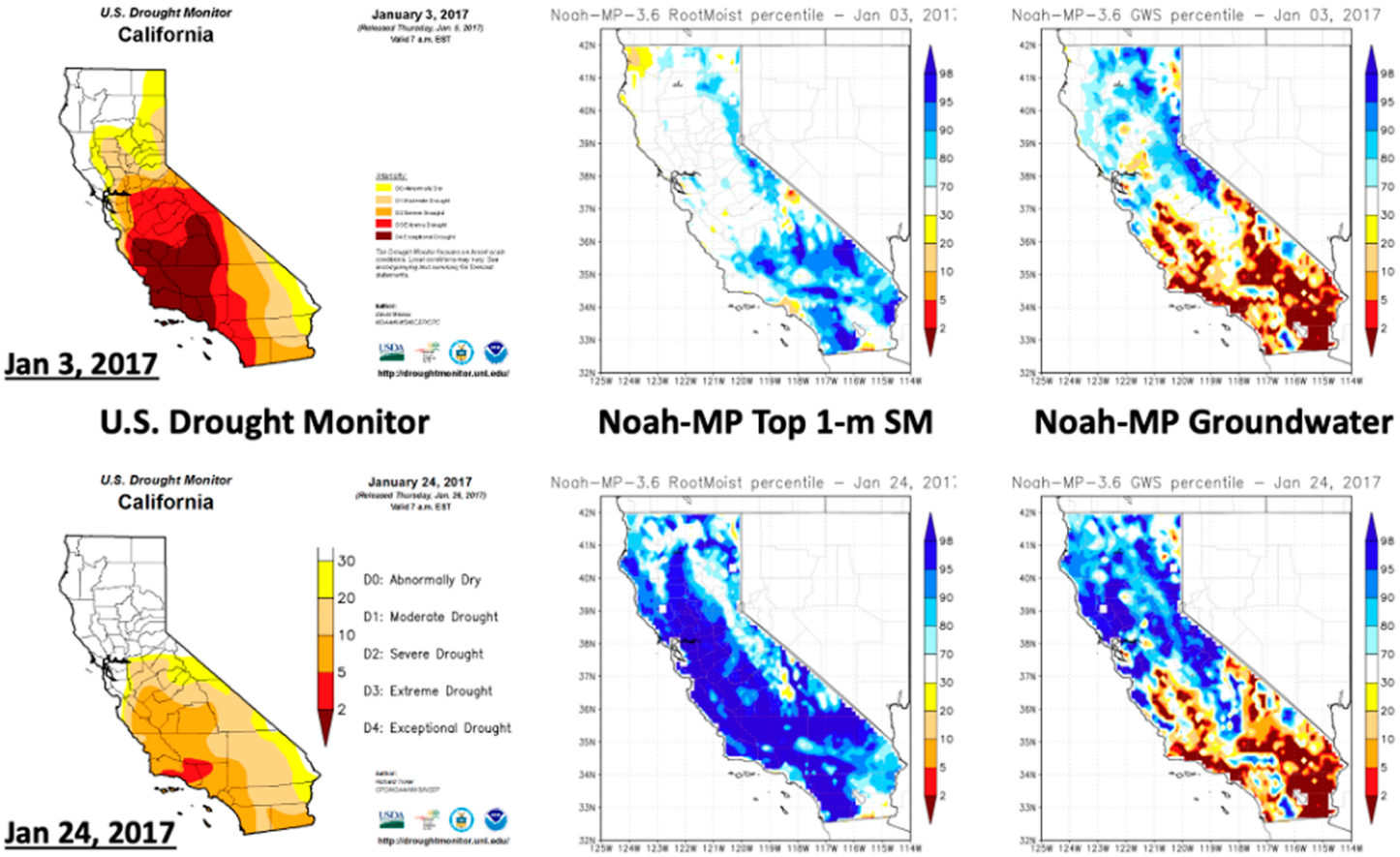

Fig. 6. Drought categories from (left) the USDM and from (center) Noah-MP simulations of top 1-m soil moisture and (right) groundwater. (top) States on 3 Jan 2017 and (bottom) states three weeks later, on 24 Jan 2017.

1-m soil moisture and groundwater storage drought severity categories for 3 January 2017 in the state of California. The USDM for this week shows exceptional drought over much of Southern California, with other drought categories over most of the state. This week was in the middle of a winter where California was starting to recover from a multiyear drought, and several atmospheric rivers had already provided significant winter precipitation. However, water storages in reservoirs and in wells (aka, groundwater) had not yet fully recovered. The Noah-MP top 1-m soil moisture percentiles show neutral to slightly wet conditions over the state, while the simulated Noah-MP groundwater percentiles show exceptional drought still in place over much of the southern half of California. The bottom row shows the same three panels (USDM, Noah-MP top 1-m soil moisture, and Noah-MP groundwater), but for three weeks later, on 24 January 2017. There were more atmospheric river events during these three weeks, resulting in a reduction of drought severity in the USDM. The top 1-m soil moisture is simulated to be very wet; yet the groundwater percentiles still show very dry conditions. SMAP surface soil moisture observations for this week also showed very wet surface soil moisture during this week, as did the operational NLDAS phase-2 LSMs (not shown). None of the operational NLDAS-2 LSMs currently include a representation of groundwater physics. The USDM author, in the National Drought Summary for 24 January 2017 (https://droughtmonitor.unl.edu/services/data/summary/html/usdm_summary_20170124.html), cited continuing observations of dry well measurements as justification for the continuation of severe drought conditions over Southern California for this week. The slower recovery of the groundwater storage in the Noah-MP LSM despite very wet top 1-m soils demonstrates the important role of groundwater in assessing drought recovery. This has been recognized in the USDM community, who have incorporated GRACE-based drought monitoring indicators into their weekly products (Houborg et al. 2012).

It should be kept in mind that adding model physics inherently increases the model complexity, adding parameters that can sometime not be directly observable. For instance, for groundwater, direct observations of the groundwater table might not be directly available at the particular site of interest. Dynamic phenology module requires specification of a temperature, light, and water dependence function, which might not be perfect, causing uncertainties in the water cycle (Zhang et al. 2019). Finally, one should not overlook the essential role of humans on land management (Wheater and Evans 2009) or on groundwater abstraction (Döll et al. 2014). Those effects are essentially absent from current land surface models but are likely essential.

Case studies

Flash drought. In the USDM era (from 2000 to present), there have been several drought events that were notable for their rapid onset. These types of events have been termed "flash droughts," and exhibited a rapid rate of intensification. Otkin et al. (2018) proposed a definition for flash drought, and noted that they tend to occur more often in the summer due to an increase in the evaporative demand. The satellite era, which has enabled many of the observational capacities detailed in a previous section, has provided several new drought indices that can detect these rapidly emerging droughts through remote sensing.

ESI uses remotely sensed thermal-based evaporation to estimate the vegetation stress. The vegetation (or evaporative) stress, along with newer indicators like the evaporative demand drought index (EDDI; Hobbins et al. 2016) has been shown to represent rapidly emerging drought conditions, often before other drought indices or products reflect these stressed conditions (McEvoy et al. 2016; Otkin et al. 2018). The 2012 flash drought in the central United States is a particular example of this type of drought, with high temperature anomalies leading to strong drought intensification (Otkin et al. 2016; Basara et al. 2019). The ESI is also one of the inputs to the quick drought response index (QuickDRI), which is led by the National Drought

Mitigation Center at the University of Nebraska–Lincoln (Wardlow et al. 2017). QuickDRI is a shorter-term indication of dryness and is designed specifically to detect rapid-onset drought conditions.

Snow drought. Low snowpack record years are critical to droughts in snow-affected areas, such as in the west CONUS (Mao et al. 2015; Cooper et al. 2016; Dierauer et al. 2019). With growing awareness of and concerns about the impacts of climate change, there has been increased attention to snow droughts (Harpold et al. 2017). The 2013–16 California drought and its links to low snow accumulations has been of particular interest (Hatchett and McEvoy 2018). Here, the 2013–16 California snow drought is analyzed using model simulations. The study domain is the Sierra Nevada of California, defined according to Mao et al. (2015) where long-term average 1 April SWE exceeded 10 mm over the reconstructed history. This area was chosen because it is the source of water for much of California, and hence low snowpacks in this area lead to drought conditions for much of the rest of the state.

Empirical cumulative distribution functions (ECDFs) were computed for 1 April SWE (from Noah-MP BASE output), winter (November–March) accumulated precipitation *P*, and winter (November–March) average surface air temperature to assess the severity of the drought during drought years 2013–16 and other dry years. The 1 April SWE is a standard indicator of water supply in the western United States, and is correlated to the winter accumulated precipitation and surface air temperature. The ECDFs are analyzed to see how well correlated extreme drought years are between these three variables as drought indicators. As shown in Fig. 7, the years 2015, 1976, and 1977 are the most severe snow droughts based on 1 April SWE, whereas only 1976 and 1977 are the most severe droughts based on winter (November–March) precipitation. Based on winter average temperature, 2015 was among the years with a warmest winter. The six years with the lowest 1 April SWE are identified with different colors in Fig. 7. It should be noted that the second and third most severe snow droughts classified in our study are 1976 and 1977, while they are 1977 and 1976 (respectively) in Mao et al. (2015). The differences might result from the different atmospheric forcing data and models used in Mao et al. (2015) and in this study.

Analysis was also performed using 2- and 3-yr average drought conditions (see Figs. 8 and 9). For 2-yr events, combined water year 2014–2015 ranked the second most severe in terms of all three measures of SWE, winter *P*, and winter *T*. Combined water years 1976–77 form the driest 2-yr event in the record of SWE and winter *P*. For 3-yr events, combined water years 2013–15 are not exceptional in winter *P* and rank the fourth in winter *T*; however, this results in the most severe 1 April SWE. The results of 2- and 3-yr events are supported by Mao et al. (2015).

Compound droughts and heat waves. Droughts and heat waves rarely occur in isolation, rather they should be thought of as compound extreme events (Zscheischler and Seneviratne 2017; Zhou et al. 2019a,b) in which heat waves and soil moisture and droughts are strongly interacting. Indeed, initial soil moisture deficit reduces evapotranspiration and increases sensible heat flux, thus warming and drying the atmospheric boundary layer (Zhou et al. 2019a), leading to the onset or maintenance of a heat wave. Similarly, an initial heat wave rapidly depletes soil moisture, leading (if sustained) to a soil moisture drought.

Discussion and conclusions

Advances in observations and models, coupled with new understanding about physical mechanisms and feedbacks controlling the development, duration, and recovery from drought have led to substantial growth in potential drought indicators. Many of these "newer" indicators (e.g., NLDAS soil moisture percentiles, ESI, GRACE-based groundwater

percentiles) are being routinely considered as part of the USDM (Svoboda et al. 2002), but it is not clear which indicators receive the most weight nor how these weights have changed over time to reflect the unique information provided by the various indicators. Currently funded work by NIDIS is attempting to quantify these changes by estimating these weights via machine learning.

The drought reconstruction presented here shows that the choices of indicators and land surface model physics strongly affect the estimates of drought onset, intensity, and duration. For example, when using dynamic vegetation, these droughts tend to have smaller spatial coverage and average severity. Although not shown here, the more comprehensive analysis of Su et al. (2021) suggests that groundwater parameterizations can lead to longer temporal durations, which might be especially important for predicting recovery. Further, standard

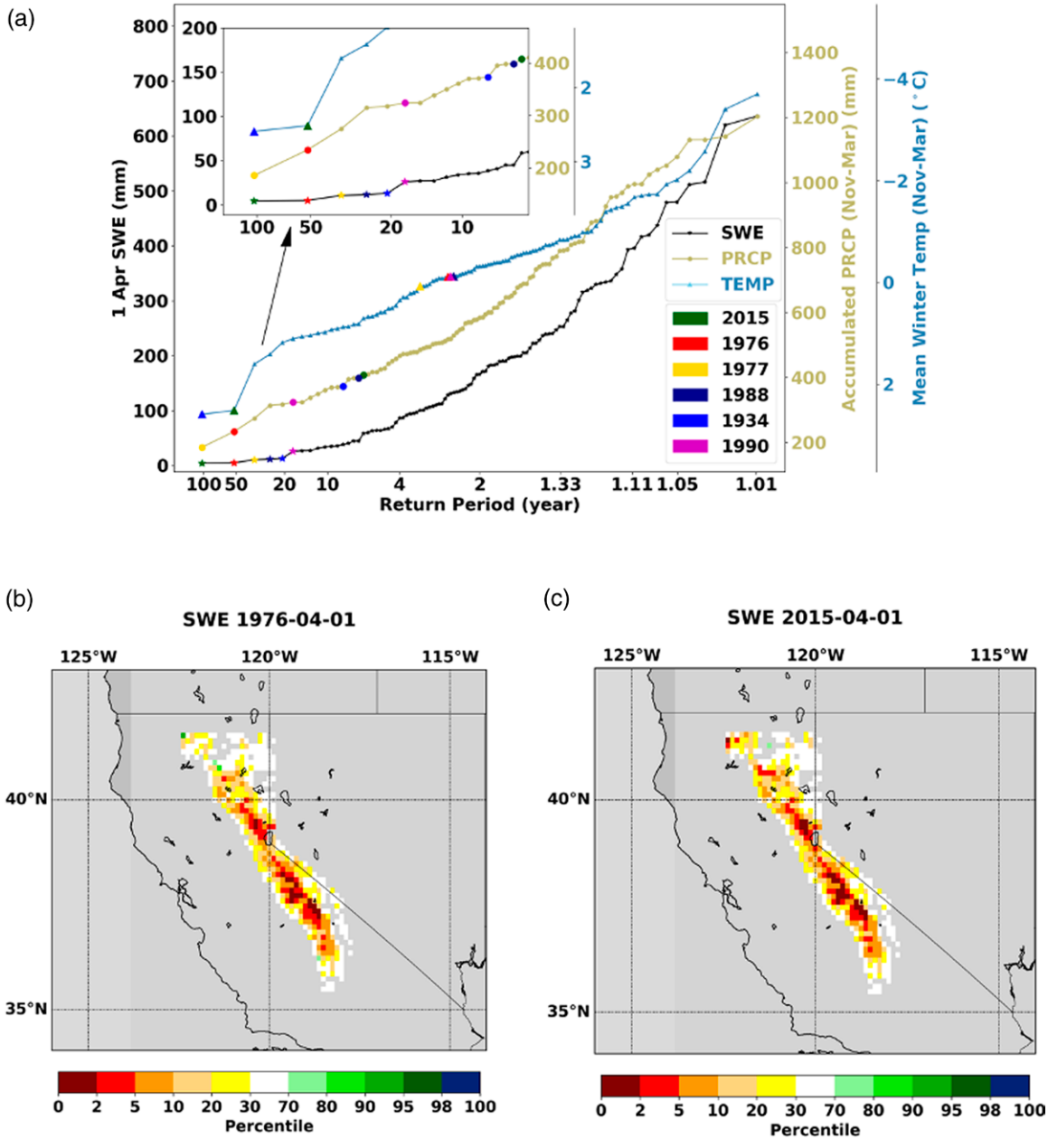

Fig. 7. (a) ECDFs of aggregate winter precipitation (khaki dot line), simulated aggregate 1 Apr SWE (black stars line), and averaged winter surface air temperature (sky-blue triangle line) for water year 1915–2018. The six years with the lowest SWE values are labeled. The Apr SWE percentile relative to 1916–2018 for SWE drought years (b) 1976 and (c) 2015.

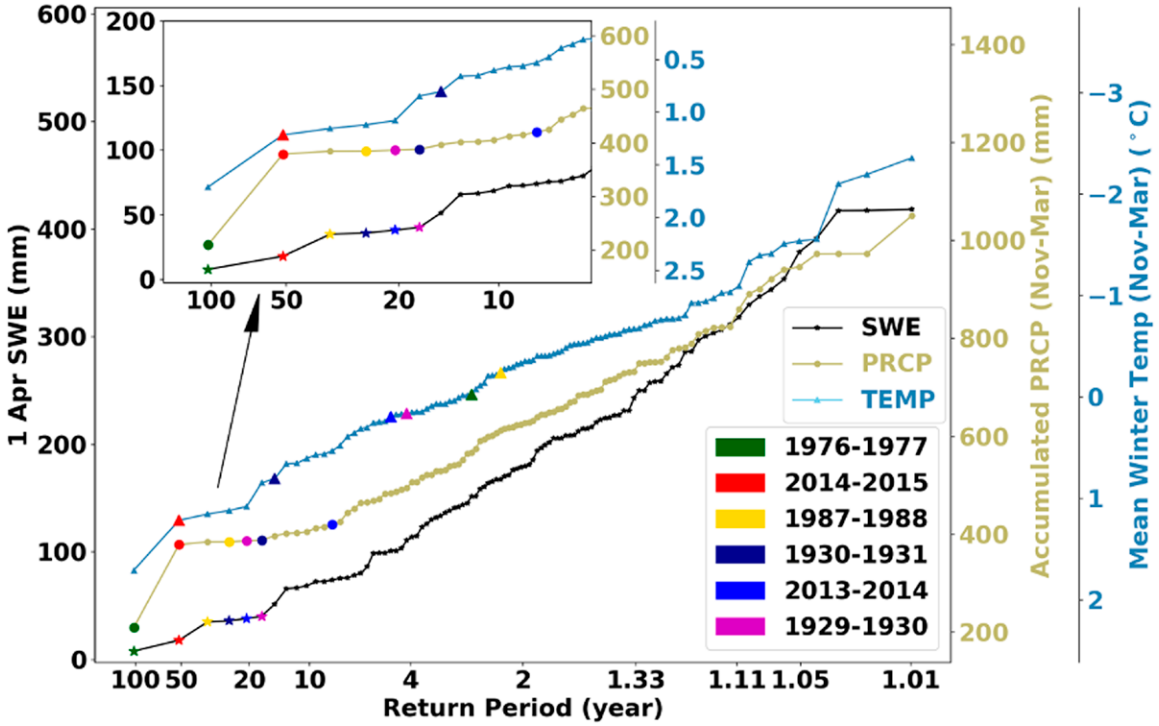

Fig. 8. As in Fig. 7a, but as an average for 2-yr events.

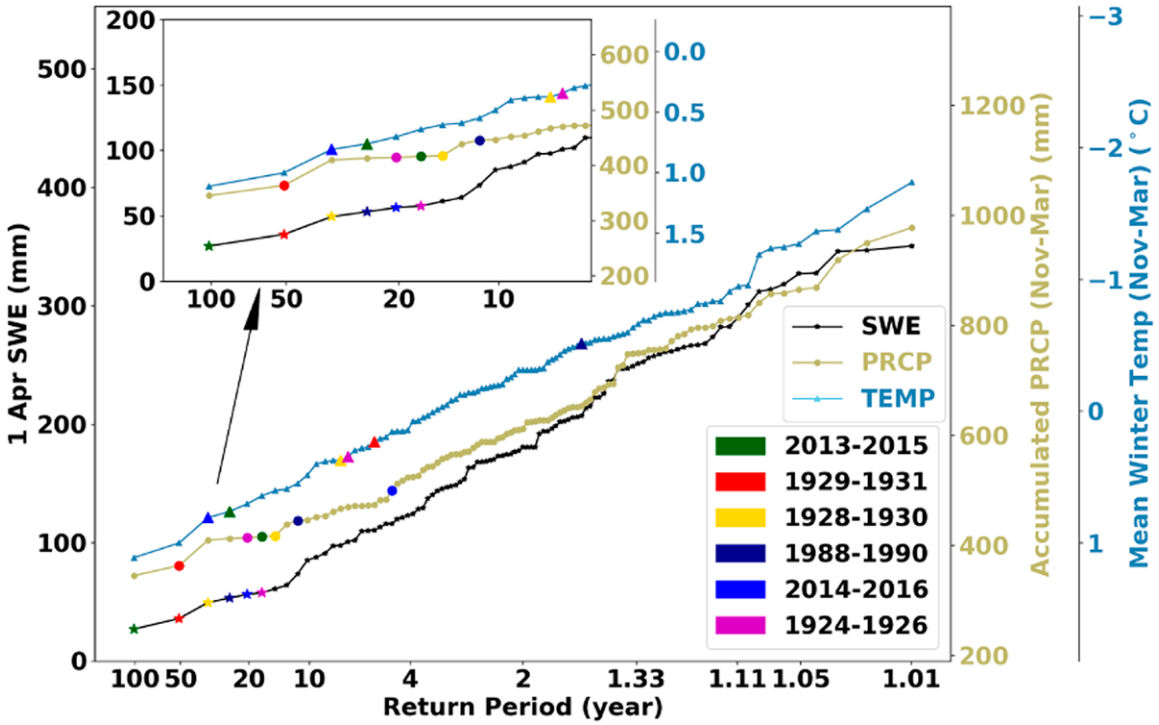

Fig. 9. As in Fig. 7a, but as an average for 3-yr events.

indicators should be augmented with newer indicators such as EDDI and remotely sensed indicators such as ESI or QuickDRI for flash droughts, and alternative indicators such as 1 April SWE for snow-dominated areas.

Beyond model physics and drought indicators, emerging understanding of the role of multiple driving factors in influencing drought development and duration is leading to the notion of compound hazards, such as droughts and heat waves (Zscheischler et al. 2018;

Sadegh et al. 2018; Zhou et al. 2019a). This understanding suggests that drought management requires multifaceted information about impacts across ecosystems, water resources, and different economic sectors. Efforts such as the USDM Drought Impacts Reporter (Smith et al. 2014) helps reduce vulnerability to drought by enabling planners to better target actions. Advances in drought monitoring and prediction, including a better understanding of processes and indicators, are supporting drought management for the twenty-first century.

Acknowledgments. All the authors were supported by the NOAA Modeling and Predictions Program and are members of the NOAA MAPP Drought Task Force. C.D.P-L. and D.M.M. were partially supported by NASA's Terrestrial Hydrology Program.

Data availability statement. The extended forcings used in this study are openly available at ftp://livnehpublicstorage.colorado.edu/public/sulu/extended_PrecTminTmaxWind_2012_2018/. The outputs that support the findings of this study are openly available at http://doi.org/10.6084/m9.figshare.12107154. The output data can be viewed via https://figshare.com/s/7a1c251d6ba2960468c3.

References

AghaKouchak, A., A. Farahmand, F. S. Melton, J. Teixeira, M. C. Anderson, B. D. Wardlow, and C. R. Hain, 2015: Remote sensing of drought: Progress, challenges and opportunities. *Rev. Geophys.*, **53**, 452–480, https://doi.org/10.1002/2014RG000456.

Allen, R. G., L. S. Pereira, D. Raes, and M. Smith, 1998: Crop evapotranspiration: Guidelines for computing crop water requirements. FAO Irrigation and drainage Paper 56, 300 pp.

Anderson, M. C., J. M. Norman, J. R. Mecikalski, J. A. Otkin, and W. P. Kustas, 2007: A climatological study of evapotranspiration and moisture stress across the continental United States based on thermal remote sensing: 2. Surface moisture climatology. *J. Geophys. Res.*, **112**, D11112, https://doi.org/10.1029/2006JD007507.

——, C. Hain, B. Wardlow, A. Pimstein, J. R. Mecikalski, and W. P. Kustas, 2011: Evaluation of drought indices based on thermal remote sensing of evapotranspiration over the continental United States. *J. Climate*, **24**, 2025–2044, https://doi.org/10.1175/2010JCLI3812.1.

Andreadis, K. M., E. A. Clark, A. W. Wood, A. F. Hamlet, and D. P. Lettenmaier, 2005: Twentieth-century drought in the conterminous United States. *J. Hydrometeor.*, **6**, 985–1001, https://doi.org/10.1175/JHM450.1.

Bacour, C., and Coauthors, 2019: Differences between OCO-2 and GOME-2 SIF products from a model-data fusion perspective. *J. Geophys. Res. Biogeosci.*, **124**, 3143–3157, https://doi.org/10.1029/2018JG004938.

Barbu, A. L., J. C. Calvet, J. F. Mahfouf, C. Albergel, and S. Lafont, 2011: Assimilation of soil wetness index and leaf area index into the ISBA-A-gs land surface model: Grassland case study. *Biogeosciences*, **8**, 1971–1986, https://doi.org/10.5194/bg-8-1971-2011.

Barnett, T. P., J. C. Adam, and D. P. Lettenmaier, 2005: Potential impacts of a warming climate on water availability in snow-dominated regions. *Nature*, **438**, 303–309, https://doi.org/10.1038/nature04141.

Basara, J. B., J. I. Christian, R. A. Wakefield, J. A. Otkin, E. H. Hunt, and D. P. Brown, 2019: The evolution, propagation, and spread of flash drought in the central United States during 2012. *Environ. Res. Lett.*, **14**, 084025, https://doi.org/10.1088/1748-9326/ab2cc0.

Bateni, S. M., and D. Entekhabi, 2012: Relative efficiency of land surface energy balance components. *Water Resour. Res.*, **48**, W04510, https://doi.org/10.1029/2011WR011357.

Best, M. J., and Coauthors, 2011: The Joint UK Land Environment Simulator (JULES), model description—Part I: Energy and water fluxes. *Geosci. Model Dev.*, **4**, 677–699, https://doi.org/10.5194/gmd-4-677-2011.

Bohn, T. J., B. Livneh, J. W. Oyler, S. W. Running, B. Nijssen, and D. P. Lettenmaier, 2013: Global evaluation of MTCLIM and related algorithms for forcing of ecological and hydrological models. *Agric. For. Meteor.*, **176**, 38–49, https://doi.org/10.1016/j.agrformet.2013.03.003.

Bretherton, C. S., and A. H. Sobel, 2003: The Gill model and the weak temperature gradient approximation. *J. Atmos. Sci.*, **60**, 451–460, https://doi.org/10.1175/1520-0469(2003)060<0451:TGMATW>2.0.CO;2.

Brown, J. F., B. D. Wardlow, T. Tadesse, M. J. Hayes, and B. C. Reed, 2008: The Vegetation drought response index (VegDRI): A new integrated approach for monitoring drought stress in vegetation. *GIsci. Remote Sens.*, **45**, 16–46, https://doi.org/10.2747/1548-1603.45.1.16.

Byrne, M. P., and P. A. O'Gorman, 2013: Link between land-ocean warming contrast and surface relative humidities in simulations with coupled climate models. *Geophys. Res. Lett.*, **40**, 5223–5227, https://doi.org/10.1002/grl.50971.

——, and ——, 2016: Understanding decreases in land relative humidity with global warming: Conceptual model and GCM simulations. *J. Climate*, **29**, 9045–9061, https://doi.org/10.1175/JCLI-D-16-0351.1.

Calvet, J. C., V. Rivalland, C. Picon-Cochard, and J. M. Guehl, 2004: Modelling forest transpiration and CO_2 fluxes—Response to soil moisture stress. *Agric. For. Meteor.*, **124**, 143–156, https://doi.org/10.1016/j.agrformet.2004.01.007.

Clark, D. B., and Coauthors, 2011: The Joint UK Land Environment Simulator (JULES), model description—Part II: Carbon fluxes and vegetation dynamics. *Geosci. Model Dev.*, **4**, 701–722, https://doi.org/10.5194/gmd-4-701-2011.

Cook, B. I., T. R. Ault, and J. E. Smerdon, 2015: Unprecedented 21st century drought risk in the American Southwest and Central Plains. *Sci. Adv.*, **1**, e1400082, https://doi.org/10.1126/sciadv.1400082.

Cooper, M. G., A. W. Nolin, and M. Safeeq, 2016: Testing the recent snow drought as an analog for climate warming sensitivity of Cascades snowpacks. *Environ. Res. Lett.*, **11**, 084009, https://doi.org/10.1088/1748-9326/11/8/084009.

Dai, A., 2011: Characteristics and trends in various forms of the palmer drought severity index during 1900–2008. *J. Geophys. Res.*, **116**, D12115, https://doi.org/10.1029/2010JD015541.

——, 2013: Increasing drought under global warming in observations and models. *Nat. Climate Change*, **3**, 52–58, https://doi.org/10.1038/nclimate1633.

——, K. E. Trenberth, and T. Qian, 2004: A global dataset of Palmer drought severity index for 1870–2002: Relationship with soil moisture and effects of surface warming. *J. Hydrometeor.*, **5**, 1117–1130, https://doi.org/10.1175/JHM-386.1.

Diamond, H. J., and Coauthors, 2013: U.S. Climate Reference Network after one decade of operations: Status and assessment. *Bull. Amer. Meteor. Soc.*, **94**, 485–498, https://doi.org/10.1175/BAMS-D-12-00170.1.

Dickinson, R. E., M. Shaikh, R. Bryant, L. Graumlich, R. E. Dickinson, M. Shaikh, R. Bryant, and L. Graumlich, 1998: Interactive canopies for a climate model. *J. Climate*, **11**, 2823–2836, https://doi.org/10.1175/1520-0442(1998)011<2823:ICFACM>2.0.CO;2.

Dierauer, J. R., D. M. Allen, and P. H. Whitfield, 2019: Snow drought risk and susceptibility in the western United States and southwestern Canada. *Water Resour. Res.*, **55**, 3076–3091, https://doi.org/10.1029/2018WR023229.

Döll, P., H. Müller Schmied, C. Schuh, F. T. Portmann, and A. Eicker, 2014: Global-scale assessment of groundwater depletion and related groundwater abstractions: Combining hydrological modeling with information from well observations and GRACE satellites. *Water Resour. Res.*, **50**, 5698–5720, https://doi.org/10.1002/2014WR015595.

Dorigo, W. A., and Coauthors, 2011: The International Soil Moisture Network: A data hosting facility for global in situ soil moisture measurements. *Hydrol. Earth Syst. Sci.*, **15**, 1675–1698, https://doi.org/10.5194/hess-15-1675-2011.

Doughty, R., P. Köhler, C. Frankenberg, T. S. Magney, X. Xiao, Y. Qin, X. Wu, and B. Moore, 2019: TROPOMI reveals dry-season increase of solar-induced chlorophyll fluorescence in the Amazon forest. *Proc. Natl. Acad. Sci. USA*, **116**, 22 393–22 398, https://doi.org/10.1073/pnas.1908157116.

Entekhabi, D., and Coauthors, 2010: The Soil Moisture Active Passive (SMAP) mission. *Proc. IEEE*, **98**, 704–716, https://doi.org/10.1109/JPROC.2010.2043918.

Ficklin, D. L., and K. A. Novick, 2017: Historic and projected changes in vapor pressure deficit suggest a continental-scale drying of the United States atmosphere. *J. Geophys. Res. Atmos.*, **122**, 2061–2079, https://doi.org/10.1002/2016JD025855.

Funk, C., and Coauthors, 2015: The Climate Hazards Infrared Precipitation with Stations—A new environmental record for monitoring extremes. *Sci. Data*, **2**, 150066, https://doi.org/10.1038/sdata.2015.66.

——, and Coauthors, 2019: Recognizing the Famine Early Warning Systems Network over 30 years of drought early warning science advances and partnerships promoting global food security. *Bull. Amer. Meteor. Soc.*, **100**, 1011–1027, https://doi.org/10.1175/BAMS-D-17-0233.1.

Gan, Y., X. Z. Liang, Q. Duan, F. Chen, J. Li, and Y. Zhang, 2019: Assessment and reduction of the physical parameterization uncertainty for Noah-MP land surface model. *Water Resour. Res.*, **55**, 5518–5538, https://doi.org/10.1029/2019WR024814.

Gao, B. C., 1996: NDWI—A normalized difference water index for remote sensing of vegetation liquid water from space. *Remote Sens. Environ.*, **58**, 257–266, https://doi.org/10.1016/S0034-4257(96)00067-3.

Gentine, P., P. D'Odorico, B. R. Lintner, G. Sivandran, and G. Salvucci, 2012: Interdependence of climate, soil, and vegetation as constrained by the Budyko curve. *Geophys. Res. Lett.*, **39**, L19404, https://doi.org/10.1029/2012GL053492.

——, A. Chhang, A. Rigden, and G. Salvucci, 2016: Evaporation estimates using weather station data and boundary layer theory. *Geophys. Res. Lett.*, **43**, 11 661–11 670, https://doi.org/10.1002/2016GL070819.

——, J. K. Green, M. Guérin, V. Humphrey, S. I. Seneviratne, Y. Zhang, and S. Zhou, 2019: Coupling between the terrestrial carbon and water cycles—A review. *Environ. Res. Lett.*, **14**, 083003, https://doi.org/10.1088/1748-9326/ab22d6.

Giardina, F., A. G. Konings, D. Kennedy, S. H. Alemohammad, R. S. Oliveira, M. Uriarte, and P. Gentine, 2018: Tall Amazonian forests are less sensitive to precipitation variability. *Nat. Geosci.*, **11**, 405–409, https://doi.org/10.1038/s41561-018-0133-5.

Girotto, M., G. J. M. De Lannoy, R. H. Reichle, and M. Rodell, 2016: Assimilation of gridded terrestrial water storage observations from GRACE into a land surface model. *Water Resour. Res.*, **52**, 4164–4183, https://doi.org/10.1002/2015WR018417.

Graf, T., T. Koike, X. Li, M. Hirai, and H. Tsutsui, 2006: Assimilating passive microwave brightness temperature data into a land surface model to improve the snow depth predictability. *Int. Geoscience and Remote Sensing Symp.*, Denver, CO, IEEE, 706–709, https://doi.org/10.1109/IGARSS.2006.185.

Grossiord, C., T. N. Buckley, L. A. Cernusak, K. A. Novick, B. Poulter, R. T. W. Siegwolf, J. S. Sperry, and N. G. McDowell, 2020: Plant responses to rising vapor pressure deficit. *New Phytol.*, **226**, 1550–1566, https://doi.org/10.1111/nph.16485.

Guttman, N. B., 1998: Comparing the palmer drought index and the standardized precipitation index. *J. Amer. Water Resour. Assoc.*, **34**, 113–121, https://doi.org/10.1111/j.1752-1688.1998.tb05964.x.

Hamed Alemohammad, S., and Coauthors, 2017: Water, Energy, and Carbon with Artificial Neural Networks (WECANN): A statistically based estimate of global surface turbulent fluxes and gross primary productivity using solar-induced fluorescence. *Biogeosciences*, **14**, 4101–4124, https://doi.org/10.5194/bg-14-4101-2017.

Harpold, A. A., M. Dettinger, and S. Rajagopal, 2017: Defining snow drought and why it matters. *Eos, Trans. Amer. Geophys. Union*, **98**, 15–17, https://doi.org/10.1029/2017EO068775.

Hatchett, B. J., and D. J. McEvoy, 2018: Exploring the origins of snow drought in the northern Sierra Nevada, California. *Earth Interact.*, **22**, https://doi.org/10.1175/EI-D-17-0027.1.

He, L., J. M. Chen, J. Liu, G. Mo, and J. Joiner, 2017: Angular normalization of GOME-2 sun-induced chlorophyll fluorescence observation as a better proxy of vegetation productivity. *Geophys. Res. Lett.*, **44**, 5691–5699, https://doi.org/10.1002/2017GL073708.

Heim, R. R., 2002: A review of twentieth-century drought indices used in the United States. *Bull. Amer. Meteor. Soc.*, **83**, 1149–1166, https://doi.org/10.1175/1520-0477-83.8.1149.

Hellwig, J., M. Stoelzle, and K. Stahl, 2021: Groundwater and baseflow drought responses to synthetic recharge stress tests. *Hydrol. Earth Syst. Sci.*, **25**, 1053–1068, https://doi.org/10.5194/hess-25-1053-2021.

Helm, L. T., H. Shi, M. Lerdau, and X. Yang, 2020: Solar-induced chlorophyll fluorescence and short-term photosynthetic response to drought. *Ecol. Appl.*, **30**, e02101, https://doi.org/10.1002/eap.2101.

Hobbins, M. T., A. Wood, D. J. McEvoy, J. L. Huntington, C. Morton, M. Anderson, and C. Hain, 2016: The evaporative demand drought index. Part I: Linking drought evolution to variations in evaporative demand. *J. Hydrometeor.*, **17**, 1745–1761, https://doi.org/10.1175/JHM-D-15-0121.1.

Hoerling, M., J. Eischeid, A. Kumar, R. Leung, A. Mariotti, K. Mo, S. Schubert, and R. Seager, 2014: Causes and predictability of the 2012 Great Plains drought. *Bull. Amer. Meteor. Soc.*, **95**, 269–282, https://doi.org/10.1175/BAMS-D-13-00055.1.

Hou, A. Y., and Coauthors, 2014: The Global Precipitation Measurement Mission. *Bull. Amer. Meteor. Soc.*, **95**, 701–722, https://doi.org/10.1175/BAMS-D-13-00164.1.

Houborg, R., M. Rodell, B. Li, R. Reichle, and B. F. Zaitchik, 2012: Drought indicators based on model-assimilated Gravity Recovery and Climate Experiment (GRACE) terrestrial water storage observations. *Water Resour. Res.*, **48**, W07525, https://doi.org/10.1029/2011WR011291.

Hsu, K., X. Gao, S. Sorooshian, H. V. Gupta, K. Hsu, X. Gao, S. Sorooshian, and H. V. Gupta, 1997: Precipitation estimation from remotely sensed information using artificial neural networks. *J. Appl. Meteor.*, **36**, 1176–1190, https://doi.org/10.1175/1520-0450(1997)036<1176:PEFRSI>2.0.CO;2.

Huffman, G. J., and Coauthors, 1997: The Global Precipitation Climatology Project (GPCP) combined precipitation dataset. *Bull. Amer. Meteor. Soc.*, **78**, 5–20, https://doi.org/10.1175/1520-0477(1997)078<0005:TGPCPG>2.0.CO;2.

——, and Coauthors, 2007: The TRMM Multisatellite Precipitation Analysis (TMPA): Quasi-global, multiyear, combined-sensor precipitation estimates at fine scales. *J. Hydrometeor.*, **8**, 38–55, https://doi.org/10.1175/JHM560.1.

——, D. T. Bolvin, D. Braithwaite, K. Hsu, R. Joyce, C. Kidd, E. J. Nelkin, and P. Xie, 2015: NASA Global Precipitation Measurement (GPM) Integrated Multi-Satellite Retrievals for GPM (IMERG). NASA GPM Algorithm Theoretical Basis Doc., version 4.5, 26 pp.

Jiang, Z., A. R. Huete, K. Didan, and T. Miura, 2008: Development of a two-band enhanced vegetation index without a blue band. *Remote Sens. Environ.*, **112**, 3833–3845, https://doi.org/10.1016/j.rse.2008.06.006.

Joiner, J., Y. Yoshida, A. P. Vasilkov, E. M. Middleton, P. K. E. Campbell, Y. Yoshida, A. Kuze, and L. A. Corp, 2012: Filling-in of near-infrared solar lines by terrestrial fluorescence and other geophysical effects: Simulations and space-based observations from SCIAMACHY and GOSAT. *Atmos. Meas. Tech.*, **5**, 809–829, https://doi.org/10.5194/amt-5-809-2012.

——, and Coauthors, 2013: Global monitoring of terrestrial chlorophyll fluorescence from moderate-spectral-resolution near-infrared satellite measurements: Methodology, simulations, and application to GOME-2. *Atmos. Meas. Tech.*, **6**, 2803–2823, https://doi.org/10.5194/amt-6-2803-2013.

Joyce, R. J., and P. Xie, 2011: Kalman filter–based CMORPH. *J. Hydrometeor.*, **12**, 1547–1563, https://doi.org/10.1175/JHM-D-11-022.1.

——, J. E. Janowiak, P. A. Arkin, and P. Xie, 2004: CMORPH: A method that produces global precipitation estimates from passive microwave and infrared data at high spatial and temporal resolution. *J. Hydrometeor.*, **5**, 487–503, https://doi.org/10.1175/1525-7541(2004)005<0487:CAMTPG>2.0.CO;2.

Kendall, M. G., *Rank Correlation Methods*. 4th ed. Charles Griffin, 272 pp.

Kennedy, D., S. Swenson, K. W. Oleson, D. M. Lawrence, R. Fisher, A. C. Lola da Costa, and P. Gentine, 2019: Implementing plant hydraulics in the Community Land Model, version 5. *J. Adv. Model. Earth Syst.*, **11**, 485–513, https://doi.org/10.1029/2018MS001500.

Kerr, Y. H., P. Waldteufel, J. P. Wigneron, J. M. Martinuzzi, J. Font, and M. Berger, 2001: Soil moisture retrieval from space: The Soil Moisture and Ocean Salinity (SMOS) mission. *IEEE Trans. Geosci. Remote Sens.*, **39**, 1729–1735, https://doi.org/10.1109/36.942551.

Keyantash, J., and J. A. Dracup, 2002: The quantification of drought: An evaluation of drought indices. *Bull. Amer. Meteor. Soc.*, **83**, 1167–1180, https://doi.org/10.1175/1520-0477-83.8.1167.

Köhler, P., L. Guanter, and C. Frankenberg, 2015: Simplified physically based retrieval of sun-induced chlorophyll fluorescence from GOSAT data. *IEEE Geosci. Remote Sens. Lett.*, **12**, 1446–1450, https://doi.org/10.1109/LGRS.2015.2407051.

Konings, A. G., and P. Gentine, 2017: Global variations in ecosystem-scale isohydricity. *Global Change Biol.*, **23**, 891–905, https://doi.org/10.1111/gcb.13389.

——, and M. Momen, 2018: Frequency-dependence of vegetation optical depth-derived isohydriciy estimates. *Int. Geoscience and Remote Sensing Symp.*, Valencia, Spain, IEEE, 9045–9047, https://doi.org/10.1109/IGARSS.2018.8519441.

——, A. P. Williams, and P. Gentine, 2017: Sensitivity of grassland productivity to aridity controlled by stomatal and xylem regulation. *Nat. Geosci.*, **10**, 284–288, https://doi.org/10.1038/ngeo2903.

Kumar, S. V., and Coauthors, 2016: Assimilation of gridded GRACE terrestrial water storage estimates in the North American Land Data Assimilation System. *J. Hydrometeor.*, **17**, 1951–1972, https://doi.org/10.1175/JHM-D-15-0157.1.

Kummerow, C., and Coauthors, 2000: The status of the Tropical Rainfall Measuring Mission (TRMM) after two years in orbit. *J. Appl. Meteor.*, **39**, 1965–1982, https://doi.org/10.1175/1520-0450(2001)040<1965:TSOTTR>2.0.CO;2.

Lawrence, D. M., and Coauthors, 2019: The Community Land Model version 5: Description of new features, benchmarking, and impact of forcing uncertainty. *J. Adv. Model. Earth Syst.*, **11**, 4245–4287, https://doi.org/10.1029/2018MS001583.

Lemordant, L., and P. Gentine, 2019: Vegetation response to rising CO_2 impacts extreme temperatures. *Geophys. Res. Lett.*, **46**, 1383–1392, https://doi.org/10.1029/2018GL080238.

——, ——, A. S. Swann, B. I. Cook, and J. Scheff, 2018: Critical impact of vegetation physiology on the continental hydrologic cycle in response to increasing CO_2. *Proc. Natl. Acad. Sci. USA*, **115**, 4093–4098, https://doi.org/10.1073/pnas.1720712115.

Li, B., and Coauthors, 2019: Global GRACE data assimilation for groundwater and drought monitoring: Advances and challenges. *Water Resour. Res.*, **55**, 7564–7586, https://doi.org/10.1029/2018WR024618.

Li, D., M. Pan, Z. Cong, L. Zhang, and E. Wood, 2013: Vegetation control on water and energy balance within the Budyko framework. *Water Resour. Res.*, **49**, 969–976, https://doi.org/10.1002/wrcr.20107.

Li, X., and Coauthors, 2018: Solar-induced chlorophyll fluorescence is strongly correlated with terrestrial photosynthesis for a wide variety of biomes: First global analysis based on OCO-2 and flux tower observations. *Global Change Biol.*, **24**, 3990–4008, https://doi.org/10.1111/gcb.14297.

Li, Y., J. Shi, and T. Zhao, 2015: Effective vegetation optical depth retrieval using microwave vegetation indices from WindSat data for short vegetation. *J. Appl. Remote Sens.*, **9**, 096003, https://doi.org/10.1117/1.JRS.9.096003.

Liu, Y. Y., R. A. M. de Jeu, M. F. McCabe, J. P. Evans, and A. I. J. M. van Dijk, 2011: Global long-term passive microwave satellite-based retrievals of vegetation optical depth. *Geophys. Res. Lett.*, **38**, L18402, https://doi.org/10.1029/2011GL048684.

Livneh, B., E. A. Rosenberg, C. Lin, B. Nijssen, V. Mishra, K. M. Andreadis, E. P. Maurer, and D. P. Lettenmaier, 2013: A long-term hydrologically based dataset of land surface fluxes and states for the conterminous United States: Update and extensions. *J. Climate*, **26**, 9384–9392, https://doi.org/10.1175/JCLI-D-12-00508.1.

Lu, Y., R. A. Duursma, C. E. Farrior, B. E. Medlyn, and X. Feng, 2020: Optimal stomatal drought response shaped by competition for water and hydraulic risk can explain plant trait covariation. *New Phytol.*, **225**, 1206–1217, https://doi.org/10.1111/nph.16207.

Maes, W. H., P. Gentine, N. E. C. Verhoest, and D. G. Miralles, 2019: Potential evaporation at eddy-covariance sites across the globe. *Hydrol. Earth Syst. Sci.*, **23**, 925–948, https://doi.org/10.5194/hess-23-925-2019.

Mann, H. B., 1945: Nonparametric tests against trend. *Econometrica*, **13**, 245–259, https://doi.org/10.2307/1907187.

Mao, Y., B. Nijssen, and D. P. Lettenmaier, 2015: Is climate change implicated in the 2013–2014 California drought? A hydrologic perspective. *Geophys. Res. Lett.*, **42**, 2805–2813, https://doi.org/10.1002/2015GL063456.

Massmann, A., P. Gentine, and C. Lin, 2019: When does vapor pressure deficit drive or reduce evapotranspiration? *J. Adv. Model. Earth Syst.*, **11**, 3305–3320, https://doi.org/10.1029/2019MS001790.

McEvoy, D. J., J. L. Huntington, M. T. Hobbins, A. Wood, C. Morton, M. Anderson, and C. Hain, 2016: The evaporative demand drought index. Part II: CONUS-wide assessment against common drought indicators. *J. Hydrometeor.*, **17**, 1763–1779, https://doi.org/10.1175/JHM-D-15-0122.1.

McKee, T. B., N. J. Doesken, and J. Kleist, 1993: The relationship of drought frequency and duration to time scales. *Proc. Eighth Conf. on Applied Climatology*, Anaheim, CA, Amer. Meteor. Soc., 179–186.

——, ——, and ——, 1995: Drought monitoring with multiple time scales. *Proc. Ninth Conf. on Applied Climatology*, Dallas TX, Amer. Meteor. Soc., 233–236.

Medlyn, B. E., and Coauthors, 2011: Reconciling the optimal and empirical approaches to modelling stomatal conductance. *Global Change Biol.*, **17**, 2134–2144, https://doi.org/10.1111/j.1365-2486.2010.02375.x.

Milly, P. C. D., and K. A. Dunne, 2016: Potential evapotranspiration and continental drying. *Nat. Climate Change*, **6**, 946–949, https://doi.org/10.1038/nclimate3046.

Mitchell K. E., and Coauthors, 2004: The multi-institution North American Land Data Assimilation System (NLDAS): Utilizing multiple GCIP products and partners in a continental distributed hydrological modeling system. *J. Geophys. Res. Atmos.*, **109**, 1–32, https://doi.org/10.1029/2003JD003823.

Mo, K. C., 2008: Model-based drought indices over the United States. *J. Hydrometeor.*, **9**, 1212–1230, https://doi.org/10.1175/2008JHM1002.1.
——, and D. P. Lettenmaier, 2015: Heat wave flash droughts in decline. *Geophys. Res. Lett.*, **42**, 2823–2829, https://doi.org/10.1002/2015GL064018.
——, and ——, 2016: Precipitation deficit flash droughts over the United States. *J. Hydrometeor.*, **17**, 1169–1184, https://doi.org/10.1175/JHM-D-15-0158.1.
——, and ——, 2018: Drought variability and trends over the central United States in the instrumental record. *J. Hydrometeor.*, **19**, 1149–1166, https://doi.org/10.1175/JHM-D-17-0225.1.
——, L. N. Long, Y. Xia, S. K. Yang, J. E. Schemm, and M. Ek, 2011: Drought indices based on the Climate Forecast System Reanalysis and ensemble NLDAS. *J. Hydrometeor.*, **12**, 181–205, https://doi.org/10.1175/2010JHM1310.1.
Mocko, D. M., S. V. Kumar, C. D. Peters-Lidard, and S. Wang, 2021: Assimilation of vegetation conditions improves the representation of drought over agricultural areas. *J. Hydrometeor.*, **22**, 1085–1098, https://doi.org/10.1175/JHM-D-20-0065.1.
Monteith, J. L., 1965: Evaporation and environment. *Symp. Soc. Exp. Biol.*, **19**, 205–234.
Nicolai-Shaw, N., J. Zscheischler, M. Hirschi, L. Gudmundsson, and S. I. Seneviratne, 2017: A drought event composite analysis using satellite remote-sensing based soil moisture. *Remote Sens. Environ.*, **203**, 216–225, https://doi.org/10.1016/j.rse.2017.06.014.
Nie, W., B. F. Zaitchik, M. Rodell, S. V. Kumar, K. R. Arsenault, B. Li, and A. Getirana, 2019: Assimilating GRACE into a land surface model in the presence of an irrigation-induced groundwater trend. *Water Resour. Res.*, **55**, 11 274–11 294, https://doi.org/10.1029/2019WR025363.
Niu, G.-Y., Z.-L. Yang, R. E. Dickinson, L. E. Gulden, and H. Su, 2007: Development of a simple groundwater model for use in climate models and evaluation with Gravity Recovery and Climate Experiment data. *J. Geophys. Res.*, **112**, D07103, https://doi.org/10.1029/2006JD007522.
——, and Coauthors, 2011: The community Noah land surface model with multiparameterization options (Noah-MP): 1. Model description and evaluation with local-scale measurements. *J. Geophys. Res.*, **116**, D12109, https://doi.org/10.1029/2010JD015139.
——, Y.-H. Fang, L.-L. Chang, J. Jin, H. Yuan, and X. Zeng, 2020: Enhancing the Noah-MP's ecosystem response to droughts with an explicit representation of plant water storage supplied by root water uptake. *J. Adv. Model. Earth Syst.*, **12**, e2020MS002062, https://doi.org/10.1029/2020MS002062.
Novick, K. A., and Coauthors, 2016: The increasing importance of atmospheric demand for ecosystem water and carbon fluxes. *Nat. Climate Change*, **6**, 1023–1027, https://doi.org/10.1038/nclimate3114.
——, A. G. Konings, and P. Gentine, 2019: Beyond soil water potential: An expanded view on isohydricity including land–atmosphere interactions and phenology. *Plant Cell Environ.*, **42**, 1802–1815, https://doi.org/10.1111/pce.13517.
Ojha, C., S. Werth, and M. Shirzaei, 2020: Recovery of aquifer-systems in southwest US following 2012–2015 drought: Evidence from InSAR, GRACE and groundwater level data. *J. Hydrol.*, **587**, 124943, https://doi.org/10.1016/j.jhydrol.2020.124943.
Otkin, J. A., M. C. Anderson, C. Hain, I. E. Mladenova, J. B. Basara, and M. Svoboda, 2013: Examining rapid onset drought development using the thermal infrared–based evaporative stress index. *J. Hydrometeor.*, **14**, 1057–1074, https://doi.org/10.1175/JHM-D-12-0144.1.
——, ——, ——, and M. Svoboda, 2014: Examining the relationship between drought development and rapid changes in the evaporative stress index. *J. Hydrometeor.*, **15**, 938–956, https://doi.org/10.1175/JHM-D-13-0110.1.
——, and Coauthors, 2016: Assessing the evolution of soil moisture and vegetation conditions during the 2012 United States flash drought. *Agric. For. Meteor.*, **218–219**, 230–242, https://doi.org/10.1016/j.agrformet.2015.12.065.
——, M. Svoboda, E. D. Hunt, T. W. Ford, M. C. Anderson, C. Hain, and J. B. Basara, 2018: Flash droughts: A review and assessment of the challenges imposed by rapid-onset droughts in the United States. *Bull. Amer. Meteor. Soc.*, **99**, 911–919, https://doi.org/10.1175/BAMS-D-17-0149.1.
Pagán, B., W. Maes, P. Gentine, B. Martens, and D. Miralles, 2019: Exploring the potential of satellite solar-induced fluorescence to constrain global transpiration estimates. *Remote Sens.*, **11**, 413, https://doi.org/10.3390/rs11040413.
Palmer, W. C., 1965: Meteorological Drought. U.S. Weather Bureau Res. Paper 45, 58 pp., https://www.ncdc.noaa.gov/temp-and-precip/drought/docs/palmer.pdf.
Penman, H. L., 1948: Natural evaporation from open water, bare soil and grass. *Proc. Roy. Soc.*, **193A**, 120–145, https://doi.org/10.1098/RSPA.1948.0037.
Piles, M., G. Camps-Valls, D. Chaparro, D. Entekhabi, A. G. Konings, and T. Jagdhuber, 2017: Remote sensing of vegetation dynamics in agro-ecosystems using SMAP vegetation optical depth and optical vegetation indices. *Int. Geoscience and Remote Sensing Symp.*, Fort Worth, TX, IEEE, 4346–4349, https://doi.org/10.1109/IGARSS.2017.8127964.
Quiring, S. M., T. W. Ford, J. K. Wang, A. Khong, E. Harris, T. Lindgren, D. W. Goldberg, and Z. Li, 2016: The North American Soil Moisture Database: Development and applications. *Bull. Amer. Meteor. Soc.*, **97**, 1441–1459, https://doi.org/10.1175/BAMS-D-13-00263.1.
Reichle, R. H., and Coauthors, 2019: Version 4 of the SMAP level-4 soil moisture algorithm and data product. *J. Adv. Model. Earth Syst.*, **11**, 3106–3130, https://doi.org/10.1029/2019MS001729.
Rodell, M., 2012: Satellite gravimetry applied to drought monitoring. *Remote Sensing of Drought: Innovative Monitoring Approaches*, CRC Press, 261–277.
——, and Coauthors, 2004: The global land data assimilation system. *Bull. Amer. Meteor. Soc.*, **85**, 381–394. https://doi.org/10.1175/BAMS-85-3-381.
Rodríguez-Fernández, N. J., and Coauthors, 2018: An evaluation of SMOS L-band vegetation optical depth (L-VOD) data sets: High sensitivity of L-VOD to above-ground biomass in Africa. *Biogeosciences*, **15**, 4627–4645, https://doi.org/10.5194/bg-15-4627-2018.
Sabater, J. M., C. Rüdiger, J.-C. Calvet, N. Fritz, L. Jarlan, and Y. Kerr, 2008: Joint assimilation of surface soil moisture and LAI observations into a land surface model. *Agric. For. Meteor.*, **148**, 1362–1373, https://doi.org/10.1016/j.agrformet.2008.04.003.
Sadegh, M., H. Moftakhari, H. V. Gupta, E. Ragno, O. Mazdiyasni, B. Sanders, R. Matthew, and A. AghaKouchak, 2018: Multihazard scenarios for analysis of compound extreme events. *Geophys. Res. Lett.*, **45**, 5470–5480, https://doi.org/10.1029/2018GL077317.
Sarachik, E. S., and M. A. Cane, 2010: *The El Niño–Southern Oscillation Phenomenon*. Cambridge University Press, 369 pp.
Schaefer, G. L., M. H. Cosh, and T. J. Jackson, 2007: The USDA Natural Resources Conservation Service Soil Climate Analysis Network (SCAN). *J. Atmos. Oceanic Technol.*, **24**, 2073–2077, https://doi.org/10.1175/2007JTECHA930.1.
Schubert, S. D., and Coauthors, 2016: Global meteorological drought: A synthesis of current understanding with a focus on SST drivers of precipitation deficits. *J. Climate*, **29**, 3989–4019, https://doi.org/10.1175/JCLI-D-15-0452.1.
Serreze, M. C., M. P. Clark, R. L. Armstrong, D. A. McGinnis, and R. S. Pulwarty, 1999: Characteristics of the western United States snowpack from snowpack telemetry (SNOTEL) data. *Water Resour. Res.*, **35**, 2145–2160, https://doi.org/10.1029/1999WR900090.
Sheffield, J., E. F. Wood, and M. L. Roderick, 2012: Little change in global drought over the past 60 years. *Nature*, **491**, 435–438, https://doi.org/10.1038/nature11575.
——, and Coauthors, 2014: A drought monitoring and forecasting system for sub-Sahara African water resources and food security. *Bull. Amer. Meteor. Soc.*, **95**, 861–882, https://doi.org/10.1175/BAMS-D-12-00124.1.
Shukla, S., and A. W. Wood, 2008: Use of a standardized runoff index for characterizing hydrologic drought. *Geophys. Res. Lett.*, **35**, L02405, https://doi.org/10.1029/2007GL032487.
——, A. McNally, G. Husak, and C. Funk, 2014: A seasonal agricultural drought forecast system for food-insecure regions of East Africa. *Hydrol. Earth Syst. Sci.*, **18**, 3907–3921, https://doi.org/10.5194/hess-18-3907-2014.
Simpson, J., R. F. Adler, and G. R. North, 1988: A proposed Tropical Rainfall Measuring Mission (TRMM) satellite. *Bull. Amer. Meteor. Soc.*, **69**, 278–295, https://doi.org/10.1175/1520-0477(1988)069<0278:APTRMM>2.0.CO;2.

Smith, K. H., M. Svoboda, M. Hayes, H. Reges, N. Doesken, K. Lackstrom, K. Dow, and A. Brennan, 2014: Local observers fill in the details on drought impact reporter maps. *Bull. Amer. Meteor. Soc.*, **95**, 1659–1662, https://doi.org/10.1175/1520-0477-95.11.1659.

Su, L., Q. Cao, M. Xiao, D. M. Mocko, M. Barlage, D. Li, C. D. Peters-Lidard, and D. P. Lettenmaier, 2021: Drought variability over the conterminous United States for the past century. *J. Hydrometeor.*, **22**, 1153–1168, https://doi.org/10.1175/JHM-D-20-0158.1.

Sun, Y., R. Fu, R. Dickinson, J. Joiner, C. Frankenberg, L. Gu, Y. Xia, and N. Fernando, 2015: Drought onset mechanisms revealed by satellite solar-induced chlorophyll fluorescence: Insights from two contrasting extreme events. *J. Geophys. Res. Biogeosci.*, **120**, 2427–2440, https://doi.org/10.1002/2015JG003150.

——, and Coauthors, 2017: OCO-2 advances photosynthesis observation from space via solar-induced chlorophyll fluorescence. *Science*, **358**, eaam5747, https://doi.org/10.1126/science.aam5747.

Svoboda, M., 2000: An introduction to the Drought Monitor. *Drought Network News*, University of Nebraska–Lincoln, 15–20.

——, and B. Fuchs, 2017: Handbook of drought indicators and indices. WMO Rep. 1173, 52 pp.

——, and Coauthors, 2002: The Drought Monitor. *Bull. Amer. Meteor. Soc.*, **83**, 1181–1190, https://doi.org/10.1175/1520-0477-83.8.1181.

Tan, J., G. J. Huffman, D. T. Bolvin, and E. J. Nelkin, 2019: IMERG V06: Changes to the morphing algorithm. *J. Atmos. Oceanic Technol.*, **36**, 2471–2482, https://doi.org/10.1175/JTECH-D-19-0114.1.

Thomas, A. C., J. T. Reager, J. S. Famiglietti, and M. Rodell, 2014: A GRACE-based water storage deficit approach for hydrological drought characterization. *Geophys. Res. Lett.*, **41**, 1537–1545, https://doi.org/10.1002/2014GL059323.

Thornthwaite, C. W., 1948: An approach toward a rational classification of climate. *Geogr. Rev.*, **38**, 55–94, https://doi.org/10.2307/210739.

Trenberth, K. E., A. Dai, G. Van Der Schrier, P. D. Jones, J. Barichivich, K. R. Briffa, and J. Sheffield, 2014: Global warming and changes in drought. *Nat. Climate Change*, **4**, 17–22, https://doi.org/10.1038/nclimate2067.

Tucker, C. J., 1979: Red and photographic infrared linear combinations for monitoring vegetation. *Remote Sens. Environ.*, **8**, 127–150, https://doi.org/10.1016/0034-4257(79)90013-0.

Uddameri, V., S. Singaraju, and E. A. Hernandez, 2019: Is standardized precipitation index (SPI) a useful indicator to forecast groundwater droughts?—Insights from a Karst aquifer. *J. Amer. Water Resour. Assoc.*, **55**, 70–88, https://doi.org/10.1111/1752-1688.12698.

Vaglio Laurin, G., C. Vittucci, G. Tramontana, P. Ferrazzoli, L. Guerriero, and D. Papale, 2020: Monitoring tropical forests under a functional perspective with satellite-based vegetation optical depth. *Global Change Biol.*, **26**, 3402–3416, https://doi.org/10.1111/gcb.15072.

Vicente-Serrano, S. M., S. Beguería, and J. I. López-Moreno, 2010: A multiscalar drought index sensitive to global warming: The standardized precipitation evapotranspiration index. *J. Climate*, **23**, 1696–1718, https://doi.org/10.1175/2009JCLI2909.1.

Wang, S. Y. S., Y. H. Lin, R. R. Gillies, and K. Hakala, 2016: Indications for protracted groundwater depletion after drought over the Central Valley of California. *J. Hydrometeor.*, **17**, 947–955, https://doi.org/10.1175/JHM-D-15-0105.1.

Wang, X., B. Qiu, W. Li, and Q. Zhang, 2019: Impacts of drought and heatwave on the terrestrial ecosystem in China as revealed by satellite solar-induced chlorophyll fluorescence. *Sci. Total Environ.*, **693**, 133627, https://doi.org/10.1016/j.scitotenv.2019.133627.

Wardlow, B. D., M. Svoboda, T. Tadesse, M. C. Anderson, J. F. Brown, C. R. Hain, and D. M. Mocko, 2017: The quick drought response index (QuickDRI)—A new tool for monitoring rapid changes in drought conditions. *23rd Conf. on Applied Climatology,* Asheville, NC, Amer. Meteor. Soc., 8B.2, https://ams.confex.com/ams/23Applied/webprogram/Paper318533.html.

Wheater, H., and E. Evans, 2009: Land use, water management and future flood risk. *Land Use Policy*, **26**, S251–S264, https://doi.org/10.1016/j.landusepol.2009.08.019.

Wild, B., I. Teubner, L. Moesinger, and W. Dorigo, 2020: A new global gross primary production (GPP) dataset based on microwave Vegetation Optical Depth Climate Archive (VODCA). *EGU General Assembly*, Online, EGU, https://doi.org/10.5194/egusphere-egu2020-17875.

Williams, A. P., and Coauthors, 2020: Large contribution from anthropogenic warming to an emerging North American megadrought. *Science*, **368**, 314–318, https://doi.org/10.1126/science.aaz9600.

Wood, E. F., S. D. Schubert, A. W. Wood, C. D. Peters-Lidard, K. C. Mo, A. Mariotti, and R. S. Pulwarty, 2015: Prospects for advancing drought understanding, monitoring, and prediction. *J. Hydrometeor.*, **16**, 1636–1657, https://doi.org/10.1175/JHM-D-14-0164.1.

Xia, Y., and Coauthors, 2012: Continental-scale water and energy flux analysis and validation for the North American Land Data Assimilation System project phase 2 (NLDAS-2): 1. Intercomparison and application of model products. **117**, *J. Geophys. Res. Atmos.*, 1–27, https://doi.org/10.1029/2011JD016048.

——, M. B. Ek, D. Mocko, C. D. Peters-Lidard, J. Sheffield, J. Dong, and E. F. Wood, 2014a: Uncertainties, correlations, and optimal blends of drought indices from the NLDAS multiple land surface model ensemble. *J. Hydrometeor.*, **15**, 1636–1650, https://doi.org/10.1175/JHM-D-13-058.1.

——, ——, C. D. Peters-Lidard, D. Mocko, M. Svoboda, J. Sheffield, and E. F. Wood, 2014b: Application of USDM statistics in NLDAS-2: Optimal blended NLDAS drought index over the continental United States. *J. Geophys. Res.*, **119**, 2947–2965, https://doi.org/10.1002/2013JD020994.

Xiao, J., and Coauthors, 2019: Solar-induced chlorophyll fluorescence exhibits a universal relationship with gross primary productivity across a wide variety of biomes. *Global Change Biol.*, **25**, e4–e6, https://doi.org/10.1111/gcb.14565.

Yang, Z.-L., and Coauthors, 2011: The community Noah land surface model with multiparameterization options (Noah-MP): 2. Evaluation over global river basins. *J. Geophys. Res.*, **116**, D12110, https://doi.org/10.1029/2010JD015140.

Yu, L., J. Wen, C. Y. Chang, C. Frankenberg, and Y. Sun, 2019: High-resolution global contiguous SIF of OCO-2. *Geophys. Res. Lett.*, **46**, 1449–1458, https://doi.org/10.1029/2018GL081109.

Zhang, Y., J. Joiner, P. Gentine, and S. Zhou, 2018a: Reduced solar-induced chlorophyll fluorescence from GOME-2 during Amazon drought caused by dataset artifacts. *Global Change Biol.*, **24**, 2229–2230, https://doi.org/10.1111/gcb.14134.

——, ——, S. Hamed Alemohammad, S. Zhou, and P. Gentine, 2018b: A global spatially contiguous solar-induced fluorescence (CSIF) dataset using neural networks. *Biogeosciences*, **15**, 5779–5800, https://doi.org/10.5194/bg-15-5779-2018.

——, S. Zhou, P. Gentine, and X. Xiao, 2019: Can vegetation optical depth reflect changes in leaf water potential during soil moisture dry-down events? *Remote Sens. Environ.*, **234**, 111451, https://doi.org/10.1016/j.rse.2019.111451.

Zhao, M., A. Geruo, I. Velicogna, and J. S. Kimball, 2017: A global gridded dataset of GRACE drought severity index for 2002–14: Comparison with PDSI and SPEI and a case study of the Australia millennium drought. *J. Hydrometeor.*, **18**, 2117–2129, https://doi.org/10.1175/JHM-D-16-0182.1.

Zhou, S., and Coauthors, 2019a: Land–atmosphere feedbacks exacerbate concurrent soil drought and atmospheric aridity. *Proc. Natl. Acad. Sci. USA*, **116**, 18 848–18 853, https://doi.org/10.1073/pnas.1904955116.

——, Y. Zhang, A. P. Williams, and P. Gentine, 2019b: Projected increases in intensity, frequency, and terrestrial carbon costs of compound drought and aridity events. *Sci. Adv.*, **5**, eaau5740, https://doi.org/10.1126/sciadv.aau5740.

Zhou, X., Y. Yamaguchi, and S. Arjasakusuma, 2018: Distinguishing the vegetation dynamics induced by anthropogenic factors using vegetation optical depth and AVHRR NDVI: A cross-border study on the Mongolian Plateau. *Sci. Total Environ.*, **616–617**, 730–743, https://doi.org/10.1016/j.scitotenv.2017.10.253.

Zscheischler, J., and S. I. Seneviratne, 2017: Dependence of drivers affects risks associated with compound events. *Sci. Adv.*, **3**, e1700263, https://doi.org/10.1126/sciadv.1700263.

——, and Coauthors, 2018: Future climate risk from compound events. *Nat. Climate Change*, **8**, 469–477, https://doi.org/10.1038/s41558-018-0156-3.